

## Highlights

### **High-statistics pedestrian dynamics on stairways and their probabilistic fundamental diagrams**

Caspar A.S. Pouw, Alessandro Corbetta, Alessandro Gabbana, Chiel van der Laan, Federico Toschi

- High-statistics pedestrian dynamics on real-life staircases.
- Highly-accurate anonymous pedestrian tracking via 3D depth imaging and state-of-the-art computer vision.
- Phenomenological analysis via probabilistic fundamental diagrams and Eulerian fields.
- Compressibility effects, position distributions

# High-statistics pedestrian dynamics on stairways and their probabilistic fundamental diagrams

Caspar A.S. Pouw<sup>a,b,\*</sup>, Alessandro Corbetta<sup>a,c</sup>, Alessandro Gabbana<sup>a,c</sup>, Chiel van der Laan<sup>a</sup> and Federico Toschi<sup>a,c,d</sup>

<sup>a</sup> Department of Applied Physics and Science Education, Eindhoven University of Technology, De Zaale, Eindhoven, 5600 MB, Brabant, The Netherlands

<sup>b</sup> ProRail BV, Moreelsepark 2, Utrecht, 3511EP, The Netherlands

<sup>c</sup> Eindhoven Artificial Intelligence Systems Institute, Eindhoven University of Technology, De Zaale, Eindhoven, 5600 MB, Brabant, The Netherlands

<sup>d</sup> CNR-IAC, Rome, Italy

---

## ARTICLE INFO

### Keywords:

Crowd dynamics on stairways  
Probabilistic fundamental diagrams  
Eulerian fields  
Compressibility and space occupancy  
High-statistics trajectory dataset  
Real-time pedestrian tracking

## ABSTRACT

Staircases play an essential role in crowd dynamics, allowing pedestrians to flow across large multi-level public facilities such as transportation hubs, shopping malls, and office buildings. Achieving a robust quantitative understanding of pedestrian behavior in these facilities is a key societal necessity. What makes this an outstanding scientific challenge is the extreme randomness intrinsic to pedestrian behavior. Any quantitative understanding necessarily needs to be probabilistic, including average dynamics and fluctuations. To this purpose, large-scale, real-life trajectory datasets are paramount.

In this work, we analyze the data from an unprecedentedly high statistics year-long pedestrian tracking campaign, in which we anonymously collected millions of trajectories of pedestrians ascending and descending stairs within Eindhoven Central train station (The Netherlands). This has been possible thanks to a state-of-the-art, faster than real-time, computer vision approach hinged on 3D depth imaging, sensor fusion, and YOLOv7-based depth localization. We consider both free-stream conditions, i.e. pedestrians walking in undisturbed, and trafficked conditions, unidirectional/bidirectional flows. We report on Eulerian fields (density, velocity and acceleration), showing how the walking dynamics changes when transitioning from stairs to landing. We then investigate the (mutual) positions of pedestrian as density changes, considering the crowd as a “compressible” physical medium. In particular, we show how pedestrians willingly opt to occupy fewer space than available, accepting a certain degree of compressibility. This is a non-trivial physical feature of pedestrian dynamics and we introduce a novel way to quantify this effect. As density increases, pedestrians strive to keep a minimum distance  $d \approx 0.6$  m (two treads of the staircase) from the person in front of them. Finally, we establish first-of-kind fully resolved probabilistic fundamental diagrams, where we model the pedestrian walking velocity as a mixture of a slow and fast-paced component (both in non-negligible percentages and with density-dependent characteristic fluctuations). Notably, averages and modes of velocity distribution turn out to be substantially different. Our results, of which we include probabilistic parametrizations based on few variables, are key towards improved facility design and realistic simulation of pedestrians on staircases.

---

## 1. Introduction

Staircases play an essential role in crowd dynamics, allowing pedestrians flows across large multi-level public facilities such as transfer stations, airport terminals, shopping malls, and office buildings. These facilities also often represent a primary source of crowd congestion and pedestrian accidents Jackson and Cohen (1995); Templer (1995); ProRail (2021); Feliciani, Corbetta, Haghani and Nishinari (2023). Established structural regulations, e.g. European Committee for Standardization (2002), impose performance requirements on facilities, e.g. in terms of capacity and safety, that need to be satisfied with a sufficiently high probability through the lifetime of the facility (Augusti and Ciampoli, 2008). To achieve such performance-based design, a deep phenomenological understanding of the crowd behavior within and around staircases, including averages, probabilities of fluctuations, and rare events is key. A

---

\*Corresponding author

✉ c.a.s.pouw@tue.nl (C.A.S. Pouw)

ORCID(s): 0000-0002-3041-4533 (C.A.S. Pouw)

profound understanding of the probabilistic landscape can therefore empower facility managers to gauge the frequency of dangerous events, e.g. bottlenecks, and thus anticipate potential capacity reductions.

In the past decades, the study of the dynamics of pedestrian crowds has emerged as a multidisciplinary field across civil engineering Vanumu and Tiwari (2017), physics Corbetta and Toschi (2023), mathematical modeling Cristiani, Piccoli and Tosin (2014), computer science Van Toll, Triesscheijn, Kallmann, Oliva, Pelechano, Pettré and Geraerts (2016), psychology Drury (2020), and more Haghani (2021). Alongside its immediate societal relevance, the study of pedestrian crowds shares deep connections with the fundamental physics of active matter systems Corbetta and Toschi (2023). Traditionally, crowd dynamics have been studied via small-scale laboratory setups, simulation models and/or surveys. Only during the last 10 years we established the technological capacity of performing measurement campaigns in real-life conditions. Pedestrian tracking in real-life opens up the possibility to record and study the dynamics of pedestrians on a significantly larger statistical scale, surpassing conventional (experimental) datasets by several orders of magnitude. High-statistics data is vital to characterize probabilities of fluctuations and quantify rare, potentially dangerous, events. However, in real-life contexts experimental parameters, such as crowd density, are not subject to deliberate specification, so measurements are inherently confined to the crowd dynamics manifested during the measurement campaign. Overhead depth sensing has emerged as an extremely robust option to this purpose, allowing for accuracy and respect of individual privacy Seer, Brändle and Ratti (2014); Corbetta, Bruno, Muntean and Toschi (2014); Willems, Corbetta, Menkovski and Toschi (2020).

In the context of pedestrian traffic, the main phenomenological modelling elements are average macroscopic relationships among crowd density and walking speed or flow. These average relations are generally dubbed fundamental diagrams (FDs, e.g., Vanumu and Tiwari (2017)). For flat grounds, fundamental diagrams have been extensively obtained in laboratory conditions considering, among others, uni- and multi-directional flows and entailing different populations (in terms, e.g., of age, geographical region, competitiveness, Cao, Lian, Chen, Yao, Song and Fang (2018); Ren, Zhang and Song (2019); Subaih, Maree, Chraibi, Awad and Zanoon (2019); Ye, Zeng, Zeng, Huang, Li, Fang and Song (2021)). FDs are key for infrastructural design, supporting, e.g., the evaluation of the capacity of a system. Yet, the dynamics of pedestrians is highly random due to, e.g., inter-subject and intra-subject variability, routing variability, presence of groups. Fundamental diagrams simplify the highly random dynamics of pedestrians with a single average. This reduction is unavoidable when experimental data is limited to small-scale datasets, for which statistical moments are far from convergence. On the other hand, recent depth-based large-scale real-life campaigns have allowed to integrate FDs with a resolved description of fluctuations Gabbana, Toschi, Ross, Haans and Corbetta (2022); Bršćić, Zanlungo and Kanda (2014), and even characterization of rare events happening, e.g., once in a thousand pedestrians Corbetta, Lee, Benzi, Muntean and Toschi (2017); Corbetta, Meeusen, Lee, Benzi and Toschi (2018). Research on spatial distributions and relative distances in crowds, often referred to as proxemics, emerged with studies investigating the relative distances between people in small, mostly stationary, social activities Hall (1966). This research expanded to include spatial analysis of the walking behavior of pedestrian social groups, as demonstrated by Moussaïd, Guillot, Moreau, Fehrenbach, Chabiron, Lemerrier, Pettré, Appert-Rolland, Degond and Theraulaz (2012), and later studied in more detail through the analysis of nearest neighbors in different flow types Cao, Sun, Chraibi and Jiang (2021). These studies rely on experimental data, typically involving only a limited number of trajectories. While field studies do exist, e.g. Zanlungo, Ikeda and Kanda (2014) who studied the spatial distribution in groups of 2 or 3 pedestrians, the extraction of pedestrian trajectories from the recordings is manual and labor-intensive. Large-statistics datasets open the possibility of systematic analyses of the crowd as a fluid Hughes (2003), considering, e.g., how the space is filled or how geometry influences the dynamics. This knowledge is key towards a quantitative physical understanding of the crowd behavior and realistic predictive simulations.

Pedestrian dynamics on staircases is a profoundly studied topic, pioneered five decades ago by, among others Fruin (1971); Predtechenskii and Milinskii (1978). They reported initial findings on the free flow velocity and established correlations between walking speed and crowd density. Since then extensive research has been devoted into the definition of FDs and in the study of the different factors effecting them, such as type of infrastructures (considering slope, tread-depth, riser height, Burghardt, Seyfried and Klingsch (2013); Wang, Ma, Lin, Sarvi and Li (2021), or especially long staircases Kretz, Grünebohm, Kessel, Klüpfel, Meyer-König and Schreckenberg (2008); Ma, Song, Tian, Lo and Liao (2012); Ronchi, Norén, Delin, Kuklane, Halder, Arias and Fridolf (2016); Chen, Hao, Wang, Wang, Liu and Lin (2018)), flow compositions (unidirectional, bidirectional, ascending, descending Chen, Lo and Ma (2017); Ye, Fang, Zeng, Wang, Lian and Cao (2023)), and cultural and personal features (age, gender, etc. Fujiyama and Tyler (2004)). Data has been collected via field studies with limited volunteers, surveys, and small-scale experiments Hankin and Wright (1958); Fruin (1971); Lam and Cheung (2000); Fujiyama and Tyler (2004); Ye, Chen, Yang and Wu (2008);

**Table 1**

Pedestrian dynamics on staircases in the literature. We report the horizontal walking speed (in free flow conditions) identified in previous studies, almost always measured in laboratory conditions, together with the magnitude of the dataset acquired. In this work, thanks to a real-life dataset including over 3 millions real-life trajectories we study at the statistical level pedestrian dynamics on staircases. Velocity distributions and fundamental diagrams turn out to have long tails due to the presence of multiple populations moving at different speed. This yield a substantial difference between the modes and the averages of the velocity distributions at all density levels. Besides, thanks to the large dataset we can investigate spatial fields of positions, velocities and accelerations and compressibility effects.

Source	Free flow mean speed (m/s)		Riser height (mm)	Tread depth (mm)	Slope (°)	# Trajectories
	Ascent	Descent				
Fruin (1971)	0.57	0.77	152	305	27.0	$\mathcal{O}(10^3)$
Fruin (1971)	0.51	0.67	178	286	32.0	$\mathcal{O}(10^3)$
Frantzich (1996)	$0.51 \pm 0.10$	$0.71 \pm 0.27$	205	225	42.3	$\mathcal{O}(10^3)$
Lam and Cheung (2000)	0.42	0.57	163	271	31.0	$\mathcal{O}(10^3)$
Fujiyama and Tyler (2004)	$0.68 - 0.77$	$0.80 - 0.91$	152	332	24.6	$\mathcal{O}(10)$
Kretz et al. (2008)	0.65	0.71	150	367	22.2	$\mathcal{O}(10^2)$
Peacock et al. (2012)	-	0.45	186	238	38.0	$\mathcal{O}(10^3)$
Ma et al. (2012)	-	0.55	150	280	28.2	$\mathcal{O}(10^2)$
Qu et al. (2014)	-	0.63	300	140	25.0	$\mathcal{O}(10^2)$
Qu et al. (2014)	0.55	-	330	157	26.1	$\mathcal{O}(10^2)$
Ronchi et al. (2016)	$0.62 - 0.75$	-	180	267	34.7	$\mathcal{O}(10^2)$
Chen et al. (2018)	$0.50 \pm 0.17$	$0.61 \pm 0.14$	160	260	32.0	$\mathcal{O}(10^2)$
Köster, Lehmborg and Kneidl (2019)	0.59	$0.64 - 0.69$	165	295	29.2	$\mathcal{O}(10)$
<b>This work</b>			<b>167</b>	<b>290</b>	<b>30.0</b>	<b><math>\mathcal{O}(10^6)</math></b>
<b>Free flow speed - average</b>	0.63	0.73				
<b>Free flow speed - mode</b>	$0.48 \pm 0.08$	$0.58 \pm 0.1$				
<b>Probabilistic fundamental diagrams</b>	Figure 10a	Figure 10b				
	Eq. (22) and Eq. (23)	Eq. (22) and Eq. (24)				
<b>Eulerian fields (positions/velocity/accelerations)</b>		Figure 5				
<b>Space occupation and compressibility effects</b>		Figures 7,8,9				

Peacock, Hoskins and Kuligowski (2012); Qu, Gao, Xiao and Li (2014); Shi, Ma, Luo, Li, Chen and Lin (2021). Leveraging on relatively limited datasets, of at most few hundred data points, all previous studies have unavoidably focused on deterministic average behaviors Ye et al. (2023). Conversely, for movement on stairs a fully resolved characterization of fluctuations, complementing the studies for level ground by Gabbana et al. (2022); Brščić et al. (2014), remains completely outstanding. The field of proxemics is also represented in the literature that studied pedestrian dynamics on staircases. Burghardt et al. (2013), for example, reports a topographical examination based on Eulerian fields using an experimental dataset featuring young German student descending a staircase. Building on this work, Ye et al. (2023) revisited the same dataset, delving deeper into spatial analyses by exploring lane formations and spatial distributions. Additionally, Xie, Tang, Zhang and Nicolas (2023) conducted a field study focusing on parent-child pairs during a brief 505 second time interval. With this work we aim to expand the literature with an in-depth spatial analysis of a truly unbiased and high-statistics trajectory dataset providing fundamental insights into pedestrian behaviors and interactions.

In this work, we perform a thorough phenomenological analysis of the statistical behavior of pedestrians moving on a staircase within Eindhoven Central Train Station (The Netherlands). To this purpose, we collect an unprecedented dataset consisting of over 3 millions trajectories, during a year long real-life pedestrian tracking campaign. We employ an anonymous depth-based overhead tracking system (cf. previous works by the authors Corbetta et al. (2017, 2018); Gabbana et al. (2022)) that, for the first time, we generalize to operate in all three dimensions.

We study both microscopic and macroscopic features of crowd flows observed from data: we analyze density patterns and interpersonal distance of pedestrians in diverse flow configurations, ranging from dilute up to highly dense conditions. We analyze how pedestrians fill the available space as their number increases: considering the physics concept of compressibility factor, we show how pedestrians fill the space, behaving differently from an ideal gas that would expand occupying all the available space. In particular, at variance with an ideal gas, we model how pedestrians operate filling all the available space. Moreover, we investigate the relationship between density and velocity under diverse flow conditions, including comparisons with experimental and theoretical literature data (cf. Table 1). Thanks to our high statistics dataset we are able to present a complete parametrization of the probability distribution function of the velocity, as a function of density.

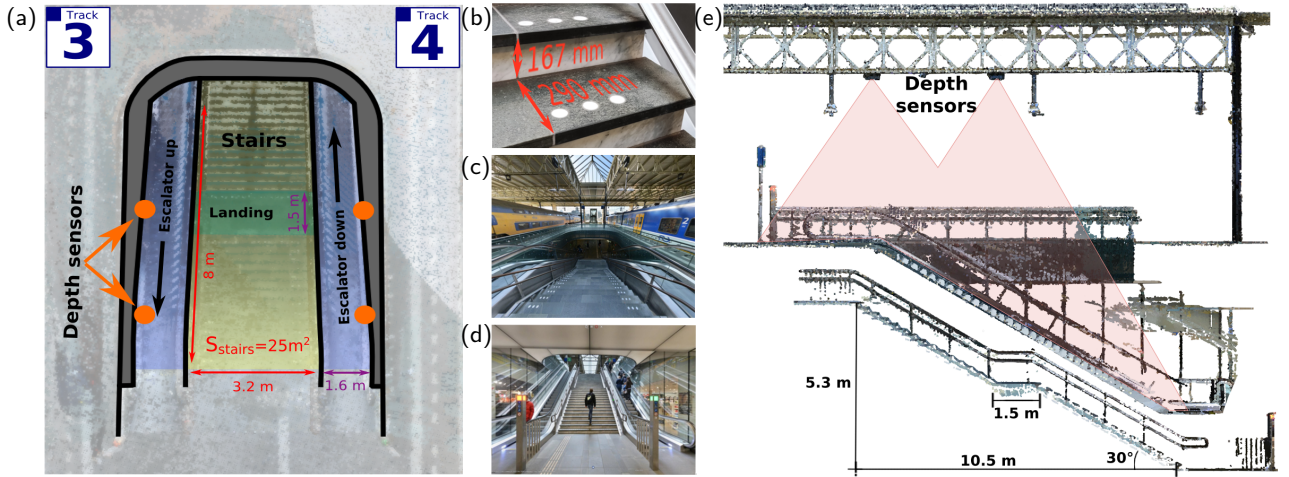


**Figure 1:** Schematic representation of the pedestrian measurement setup at Eindhoven Central Station (NL). (a) Top view of the staircase (yellow) and escalators (blue) from the perspective of the four depth sensors (orange dots). Escalator on the side of track 4 descending towards the tunnel, escalator on the side of track 3 ascending towards the platform. A staircase landing (green) is located halfway up the staircase. (b) Close-up picture of the staircase with two treads of the staircase. Each tread has rise  $h = 167$  mm and run  $r = 290$  mm (c,d) Pictures of the staircase-escalator system in (c) ascending direction, and (d) descending direction. (e) Vertical cross-section of the escalator and staircase. The depth sensors (black rectangles) are mounted to trusses on the ceiling of the train station. The sensor view cones are highlighted with a red color. The staircase and escalator both have a inclination of  $\theta = 30^\circ$ . For clarity, we applied in the image a small offset to the cross-section of the staircase.

This work is structured as follows: in Sec. 2 we describe our data acquisition campaign and measurement process. We detail the environmental setup and our depth sensors installation in Sec. 2.1. In Sec. 2.2, we report the processing pipeline which yields anonymous high-quality pedestrian trajectories based on a stream of depth images. This combines perspective corrections, sensor-fusion, state-of-the-art machine-learning-based pedestrian localization and Lagrangian tracking. We leverage specifically on a machine-learning based tracking algorithm (YOLOv7, Wang, Bochkovskiy and Liao (2022)) which enables us to achieve high quality localization even in the most crowded scenarios. In Sec. 2.3, we discuss the definition and computation of macroscopic variables, such as velocity and density, from trajectory data. In Sec. 3 we present the results of our analysis which are further organized as follows:

- In Sec. 3.1, we provide an overview of the data, detailing the most common flow conditions on the staircase. We also evaluate spatial (Eulerian) distributions of positions, velocities and accelerations to quantify the usage. We then provide a quantitative modeling of the free-stream velocity probability distribution function.
- In Sec. 3.2, we analyze interactions between pedestrians, discussing crowd compressibility effects and the relative positioning of nearest neighbors at increasingly large values of the local density.
- In Sec. 3.3 we establish a probabilistic fundamental diagram, where we describe the parametrization of the probability distribution function of the velocity, as a function of the local density.

Finally, in Sec. 4 we discuss and summarize main findings and future developments.

## 2. Pedestrian Sensing at Large Scales: from depth maps to pedestrian trajectories

### 2.1. Measurement setup at Eindhoven Train Station (NL)

The data presented in this work has been collected during a 1-year period between April 2021 and May 2022. Eindhoven Central Station (CS) is the fifth-largest train station in the Netherlands with 3 platforms and 6 train tracks. During this period of time, the station has been used on average by 46k travelers per day Spoorwegen (2023), a number

dimmed by the COVID pandemics as shown by the 77k daily users reported for the year 2019. We have continuously recorded all the movements of pedestrians traversing a highly trafficked staircase and escalator during the operational hours of the train station (6 am – 22 pm). The staircase-escalator system, Fig. 1, is the main entry point to train tracks 3 and 4. This means that its usage is highly correlated with the train schedule. Typically, boarding passengers arrive at the platform relatively scattered around the train arrival time. On the other hand, alighting passengers reach the staircase in large compact groups as soon as they leave their train.

To perform our recordings, we have developed and employed a custom system composed of a grid of four overhead depth sensors. These sensors are controlled via dedicated software performing depth recording, sensor fusion, pedestrian localization and Lagrangian tracking. The measurement campaign allowed to acquire a dataset boasting about 3 million trajectories: an average of 10 thousand per day during weekdays and 3 thousand per day during weekends. The observed staircase has a relatively narrow width of  $w_{\text{stairs}} = 3.2$  m. This makes it a notorious bottleneck for the pedestrian flow through the train station. The stairs span a total elevation change of  $h_{\text{stairs}} = 5.3$  m and a horizontal distance of  $l_{\text{stairs}} = 10.5$  m with a slope of  $\theta = 30^\circ$ . The staircase consists of two flights of stairs separated by a flat staircase landing halfway up the stairs, and with length  $l_{\text{landing}} = 1.5$  m. The individual treads have standard dimensions (rise  $h = 167$  mm, run  $r = 290$  mm), which are comparable to those from previous studies present in the literature (cf. Table 1), making the dynamics on such staircase representative for a general case. The escalators are located on either side of the staircase with a right-hand orientation. They have standard escalator dimensions rise  $h = 220$  mm, and run  $r = 400$  mm. The escalator has a slope of  $30^\circ$  and a horizontal velocity of  $v = 0.6$  m/s.

## 2.2. High-accuracy pedestrian tracking via depth-based 3D computer vision

We summarize here technical and algorithmic aspects of our pedestrian tracking system. We acquire raw data through a grid of overhead depth sensors recording at 30 frames per second. We employ Stereolabs Zed 2 sensors Stereolabs (2021), driven by Nvidia Jetson TX2 GPUs NVidia (2021). The sensors are mounted on horizontal trusses above the staircase-escalator system as presented in Fig. 1. Depth sensors measure the so-called depth (*or distance*) field, i.e. they probe the distance between each observed point and the sensor plane. This signal is typically represented and memorized in terms of gray scale images which, in our case, have resolution  $640 \times 360$  px<sup>2</sup> (cf. Fig 2). The gray level encodes distance with shades that become brighter (Fig. 2a-f) as distance increases. Zed sensors measure depth through a stereo vision approach: they acquire two simultaneous color views of the same scene from CCD sensors having a lateral offset of 12 cm. Similarly to the human brain, the two images are used to estimate distance. This distance reconstruction, generally referred to as stereo matching, is performed in real-time through the Zed API running on the local Nvidia Jetson TX2 card. We design our system in such a way that no color image (possibly privacy infringing) is explicitly downloaded from the sensors. We position the sensors in such a way that their view cone is partially overlapping. This configuration enables continuous coverage of the whole staircase area and of a volume that spans from the stairs up to the ground level plane.

Streams of depth maps are at the base of our trajectory measurement approach. The processing pipeline, applied to approximately 400 GB of depth images per day, is summarized in Fig. 3 and involves six main stages. Some of these stages have been described in previous works by the same authors Corbetta et al. (2017, 2018); Willems et al. (2020). For the sake of completeness we report in what follows on all stages.

We can formalize a depth image with the field  $(\mathbf{x}, d(\mathbf{x}))$ , which maps each pixel,  $\mathbf{x}$ , in the image with its distance  $d(\mathbf{x})$  from the camera. Streams of depth images undergo the following six stages:

1. **Height calibration** We observe that depth measurements present noise that affects the depth field uniformly and in a multiplicative way. In other terms, we measure the field  $Ad(\mathbf{x})$ , where  $A$  is a constant changing in time in dependence on the global scene illumination. We use a fixed spatial reference (depth of the platform) to normalize away the multiplicative constant  $A$  and obtain  $d(\mathbf{x})$ . This correction appears to be necessary with Zed sensors. Other sensors used by the same authors, e.g., Microsoft Kinects, did not need it.
2. **Perspective correction** We perform an axonometric transformation of the depth image, conceptually equivalent to bringing the sensor to an infinite altitude. This turns the view from conical to cylindrical and renders all the sight rays vertical and mutually parallel. For an ideal pinhole view, and up to a multiplicative constant  $C$ , this transformation re-projects a point  $\mathbf{x}$  in image space as

$$(\mathbf{x}, d(\mathbf{x})) \rightarrow (C\mathbf{x}d(\mathbf{x}), d(\mathbf{x})). \quad (1)$$

This transformation would ensure that points that are vertically aligned in space get mapped to the same location  $C\mathbf{x}d(\mathbf{x})$ .

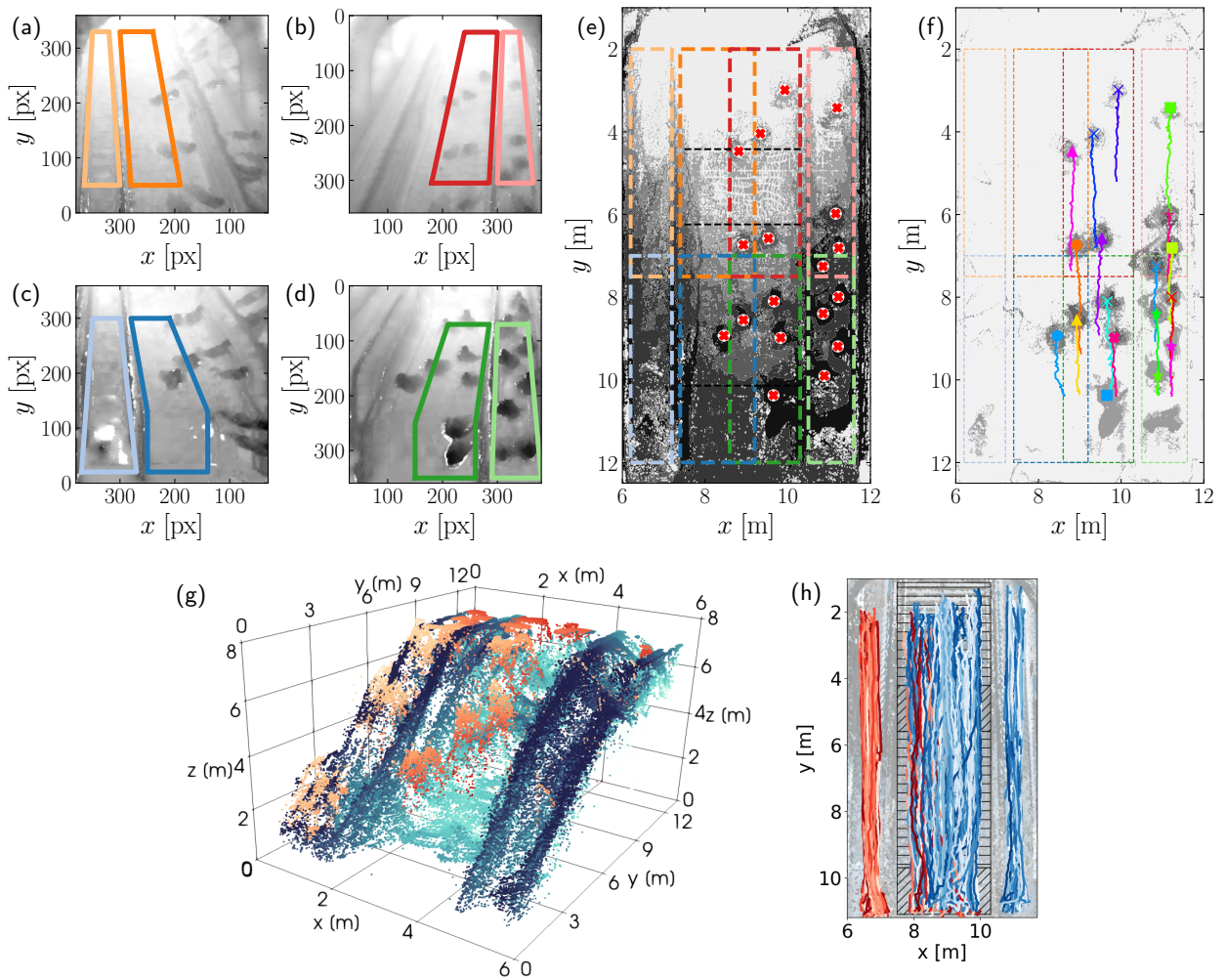


**Figure 2:** Depthmap images at different stages of the image processing. (a-d) Raw recordings of the four depth sensors. Each depth image is imposed with two regions of interest (ROI), one on the staircase (dark hue) and one on the escalator (light hue). (e, f) Depth images after perspective correction and sensor merging. From the ROIs we observe the overlapping parts of the sensor domains. We report for the pedestrian localizations in this frame together with the Lagrangian trajectories over the previous 10 seconds. (e) Without background subtraction and (f) with background subtraction. (g) 3D pointcloud of the perspective corrected and stitched depth images. The background is colored with blue tones and the foreground is colored with red tones. (h) Recorded trajectories across the staircase. Ascending trajectories are colored with a red hue and descending trajectories with a blue hue.

We observed, however, that the ideal model in Eq. (1) is still insufficient for a precise mapping of the space. This holds especially when the distance to the sensor (depth) changes significantly (i.e. moving across the stairs). To compensate on this, we consider a second order correction model:

$$(\mathbf{x}, d(\mathbf{x})) \rightarrow (\mathbf{x}, c_1 \cdot d(\mathbf{x})^2 + c_2 \cdot d(\mathbf{x}) + c_3), \quad (2)$$

with  $c_1$ ,  $c_2$  and  $c_3$  free parameters. We estimated the parameters by moving calibration targets on the scene (cardboard boxes of known size), and ensuring that the railings of the escalator, once projected with Eq. (2), remain mutually parallel.

We generate an axonometric depth image retaining for each vertically aligned point the one closest to the sensor.

- Background subtraction** To reduce localization artifacts, we retain the foreground of each depth signal. That is, only the pixels that are sufficiently closer to the sensor plane than a background estimated in absence of

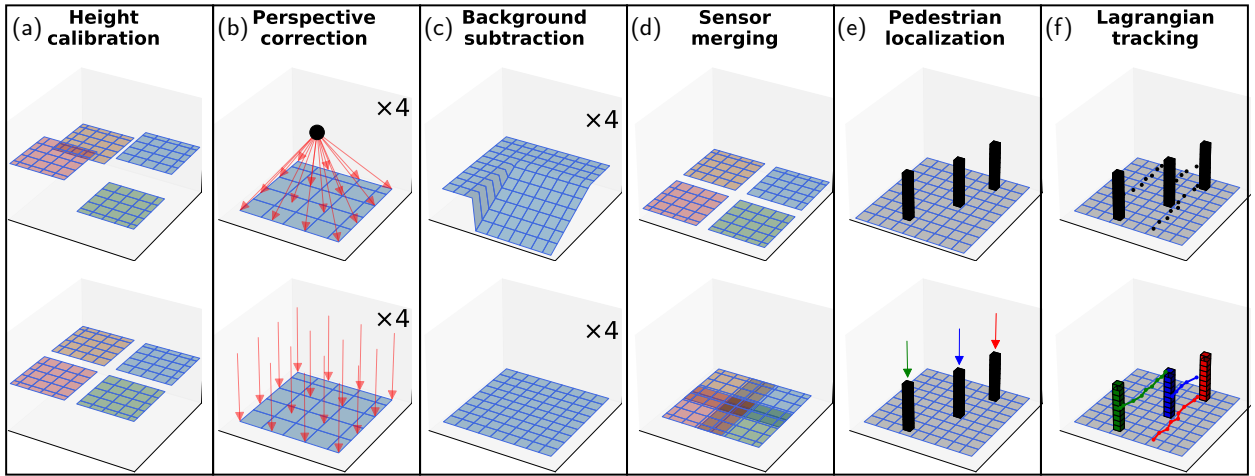


**Figure 3:** Synthetic examples of the processing steps for pedestrian tracking on inclined planes. (a) Height calibration, establishing agreement on the depth measurements. (b) Perspective correction. (c) Background subtraction. The foreground will reveal all (new) objects removing all terrain/ flattening the ground. (d) Merging all sensor images thereby creating one shared coordinate system. (e) Pedestrian localization. (f) Lagrangian time tracking.

crowding. This transformation operates as follows:

$$(\mathbf{x}, d(\mathbf{x})) \rightarrow (\mathbf{x}, d(\mathbf{x}) - \min_{\Delta t} d(\mathbf{x})), \quad (3)$$

with  $\min_{\Delta t} d(\bar{\mathbf{x}})$  the minimum depth value in the image over a small time window  $\Delta t$ . Typically, this time window is chosen in very dilute conditions to ensure the absence of crowding. In our case the background was recorded at night when the facility is closed.

4. **Depth data fusion** Having defined an axonometric view for the four depth streams, it is then possible to juxtapose them to generate a single depth image covering the entire area. In the overlapping regions, pixels with depth closest to the camera are retained. The merging is performed such to ensure that the reference cardboard boxes preserve their shape and area throughout the entire fused depth image.
5. **Localization** We perform localization using the YOLOv7 localization algorithm Wang et al. (2022). YOLO (You Only Look Once) has recently emerged as a widespread adopted algorithm for real-time object detection. Unlike traditional methods that employ multi-stage pipelines, YOLO takes a unified approach by performing object detection in a single pass. In short, a given input image gets divided into a grid and the algorithm simultaneously make predictions for bounding boxes and class probabilities for each grid cell by leveraging deep neural networks (NNs). We have trained a NN from scratch by hand-annotating depth images in an active learning fashion. In other terms, after a first annotation session (about 15 frames), we proceeded correcting the output of the localization to improve the training dataset. This has allowed for high quality tracking, outperforming previous approaches (Pouw, Willems, van Schadewijk, Thureau, Toschi and Corbetta (2022)), specially in highly dense conditions. In Table 2, we report the performance achieved by the YOLO algorithm using as test data two hours of hand-annotated depth images. We report precision, recall, and F1-score for different values of the local density. We refer the reader to Appendix A for further details.
6. **Tracking** We perform Lagrangian tracking of bounding box centroid via the Trackpy library Allan, Caswell, Keim, van der Wel and Verweij (2023). We cross-validate the obtained trajectories against the optical flow aiming at detecting false positives and tracking errors.

### 2.3. Pedestrian velocity and density: operational definitions

In this section, we define the notation and a few useful quantities, akin to those used by Saberi and Mahmassanip (2014); Hoogendoorn, Daamen, Knoop, Steenbakkens and Sarvi (2018), to guide the reader through the analysis presented in Section 3. In what follows, we will refer to the trajectory dataset, obtained following the procedure described in the previous section, with the symbol  $\mathcal{T}$ .

**Table 2**

Performance of our YOLO-based pedestrian localization algorithm against about 1000 hand-annotated frames. We report standard quality metrics: precision, recall, and F1 score. For details about the algorithm and its validation, and formal definitions of the performance metrics, see Appendix A.

Density Range (ped/m <sup>2</sup> )	True positive	False positive	False negative	Precision	Recall	F1 Score
0.55 - 0.75	373	0	2	1.0	0.9947	0.9973
0.75 - 0.95	1301	6	18	0.9954	0.9864	0.9909
0.95 - 1.15	2012	13	80	0.9936	0.9618	0.9774
1.15 - 1.35	2735	27	174	0.9902	0.9402	0.9646
1.35 - 1.55	3140	20	197	0.9937	0.9410	0.9666

We consider a coordinate system  $\mathbf{x} = (x, y)$  such that the  $x$  and  $y$  axes are, respectively, transversal and longitudinal with respect to the ascending/descending direction (cf. Fig. 2). In other terms, we consider a projection of the staircase on the horizontal plane. We denote with  $\mathbf{v}(t) = (v_x(t), v_y(t))$  the instantaneous velocity of a pedestrian, which we compute applying Savitzky-Golay filtering Savitzky and Golay (1964) on trajectory data, and likewise for the instantaneous acceleration  $\mathbf{a}(t) = (a_x(t), a_y(t))$ . Additionally, we define the frame-average walking velocity,  $v_{t,\mathcal{T}}$ , at frame,  $t$ , for a trajectory subset,  $\mathcal{T}$ :

$$v_{t,\mathcal{T}} = \frac{1}{N_{t,\mathcal{T}}} \sum_{i=1}^{N_{t,\mathcal{T}}} v_i, \quad (4)$$

with  $v_i$  the velocity of pedestrian  $i$  and  $N_{t,\mathcal{T}}$  the number of pedestrians in frame  $t$  part of subset  $\mathcal{T}$ . Due to the subset being almost obviously deductible from the context, for ease of notation we shall indicate the average velocity simply with  $v$ .

We will distinguish trajectories in our dataset,  $\mathcal{T}$ , based on two criteria:

- Direction, either downstairs or upstairs. We determine the direction by setting a threshold on the average longitudinal velocity of each trajectory,  $\langle v_y \rangle_\gamma$ . We indicate respectively with  $\mathcal{T}_\downarrow$  and  $\mathcal{T}_\uparrow$  the sets of trajectories in downstairs and upstairs direction. In formulas, it holds

$$\mathcal{T}_\downarrow = \{ \gamma \in \mathcal{T} \mid \langle v_y \rangle_\gamma < -V_t \} \quad \mathcal{T}_\uparrow = \{ \gamma \in \mathcal{T} \mid \langle v_y \rangle_\gamma > V_t \}, \quad (5)$$

with the threshold  $V_t = 0.2$  m/s.

- Movement mode, either via the stairs or via the escalators. We distinguish between the movement modes based on the position. We define the subsets  $\mathcal{T}_{\text{esc}}$  and  $\mathcal{T}_{\text{stairs}}$  as the sets consisting of trajectories with all coordinate observations located either on the escalators or on the staircase area, respectively. In formulas, these read

$$\mathcal{T}_{\text{esc}} = \{ \gamma \in \mathcal{T} \mid \mathbf{x} \in \mathcal{S}_{\text{esc}} \} \quad \mathcal{T}_{\text{stairs}} = \{ \gamma \in \mathcal{T} \mid \mathbf{x} \in \mathcal{S}_{\text{stairs}} \}. \quad (6)$$

These criteria yield four disjoint subsets

- $\mathcal{T}_{\text{stairs}\uparrow} = \mathcal{T}_{\text{stairs}} \cap \mathcal{T}_\uparrow$ , trajectories going in upstairs direction via the staircase;
- $\mathcal{T}_{\text{stairs}\downarrow} = \mathcal{T}_{\text{stairs}} \cap \mathcal{T}_\downarrow$ , trajectories going in downstairs direction via the staircase;
- $\mathcal{T}_{\text{esc}\uparrow} = \mathcal{T}_{\text{esc}} \cap \mathcal{T}_\uparrow$ , trajectories going in upstairs direction via the escalators;
- $\mathcal{T}_{\text{esc}\downarrow} = \mathcal{T}_{\text{esc}} \cap \mathcal{T}_\downarrow$ , trajectories going in downstairs direction via the escalators;

Note that this categorization excludes rare cases such as pedestrians inverting their trajectories, which will be neglected from our analysis.

We conclude this section discussing the frame by frame estimation of the density, which is crucial for the computation of the fundamental diagrams. Within the literature on pedestrian dynamics, numerous methods have been

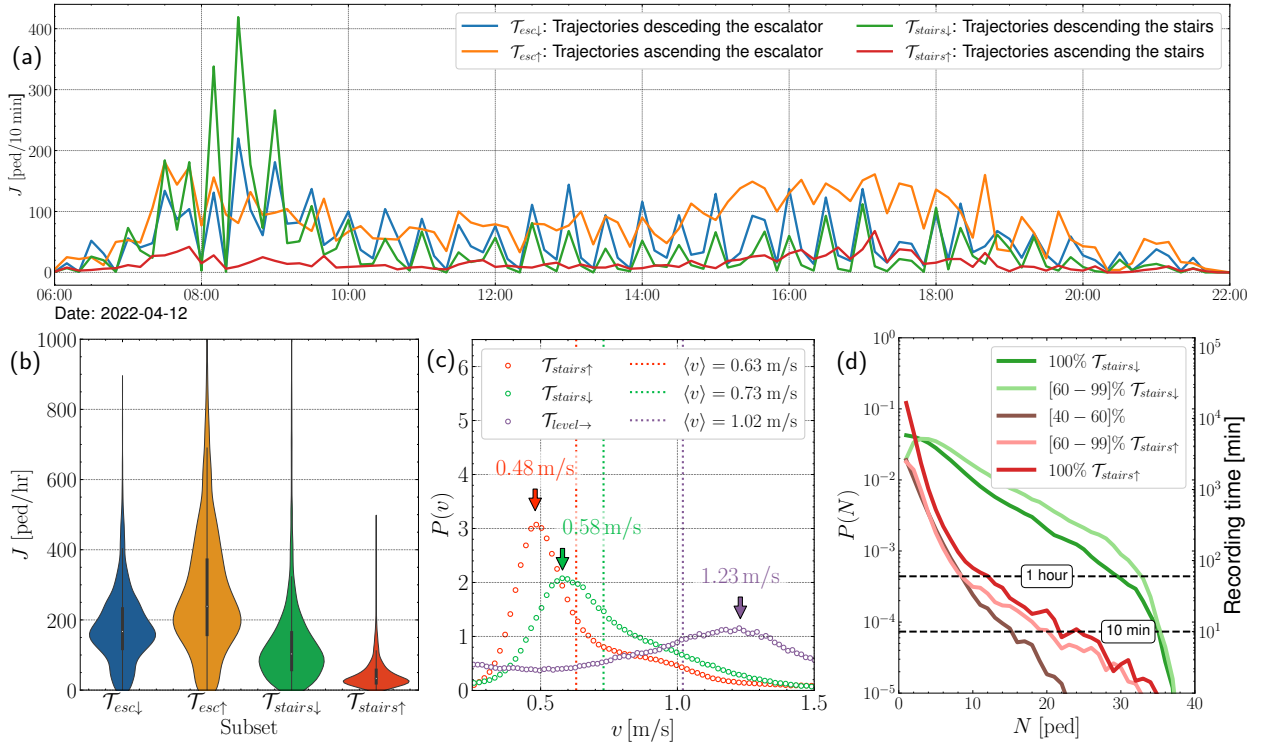


**Figure 4:** (a) Pedestrian flux,  $J$ , across the staircase ascending  $\mathcal{T}_{stairs\uparrow}$  (red) and descending  $\mathcal{T}_{stairs\downarrow}$  (green) or using the escalators to ascend  $\mathcal{T}_{esc\uparrow}$  (yellow) and descend  $\mathcal{T}_{esc\downarrow}$  (blue) per 10-minute time window for a typical working day. We observe a morning rush hour at 08:00-09:00 and afternoon rush hour 16:00-18:00. The morning is dominated by people going down to the tunnel using the stairs (green) or the escalator (blue), and the afternoon by pedestrians in the other direction going towards the platform using the escalator (orange). (b) Boxplots of the pedestrian flux,  $J$ , per movement mode in pedestrians per hour. (c) Probability distribution of the free-flow walking velocity on the staircase ascending (green) and descending (red). For comparison we also report the free-flow walking velocity on level ground,  $\mathcal{T}_{level\rightarrow}$  (purple). We annotate with arrows the most probable walking velocities i.e.  $v_{stairs\uparrow} = 0.48$  m/s,  $v_{stairs\downarrow} = 0.58$  m/s and  $v_{level\rightarrow} = 1.23$  m/s. (d) Probability distribution of the flow dynamics as a function of the stairs occupation  $N$ . We report five possible flow dynamics: (1) unidirectional flows descending 100%  $\mathcal{T}_{stairs\downarrow}$  (green) and (2) ascending 100%  $\mathcal{T}_{stairs\uparrow}$  (red) (3) unbalanced bidirectional flows dominated by descending pedestrians [60 – 99]%  $\mathcal{T}_{stairs\downarrow}$  (light green) and (4) dominated by ascending [60 – 99]%  $\mathcal{T}_{stairs\uparrow}$  (light red), and (5) balanced bidirectional flow (brown) with a [40 – 60]% ratio between ascending and descending. We observe on the staircase mainly unidirectional and unbalanced bidirectional flows in the descending direction. We employ a second y axis on the right side of the figure with the recording times in minutes to indicate the size of the data for each of the five possible flow dynamics. Additionally, we impose two horizontal lines signalling thresholds for 10 minutes and 1 hour of recordings respectively. For descending motions we have significant recordings ( $> 10$  min) for pedestrian occupancy up to  $N < 35$ . For descending motion however we have few recordings for values of  $N > 20$  pedestrians.

introduced to estimate pedestrian density. For a comprehensive comparison of these methods, we refer to Steffen and Seyfried (2010); Zhang, Klingsch, Schadschneider and Seyfried (2011); Duives, Daamen and Hoogendoorn (2015). Traditionally, the pedestrian density  $\rho$  has been computed using the hydrodynamic definition:

$$\rho = \frac{N}{\bar{S}}, \quad (7)$$

where  $N$  is the number of pedestrians in the observation area  $\bar{S}$  (e.g., Steffen and Seyfried (2010); Fruin (1971)). This definition provides robust estimates in case of spatially uniform flows over surfaces much larger than the pedestrian diameter (i.e. as the continuum limit approximation becomes accurate). On the other hand, this definition strongly depends on the size of the measurement area,  $\bar{S}$ , Zhang et al. (2011), while averaging out local density fluctuations. These issues have been circumvented considering a Voronoi tessellation centered in the pedestrians

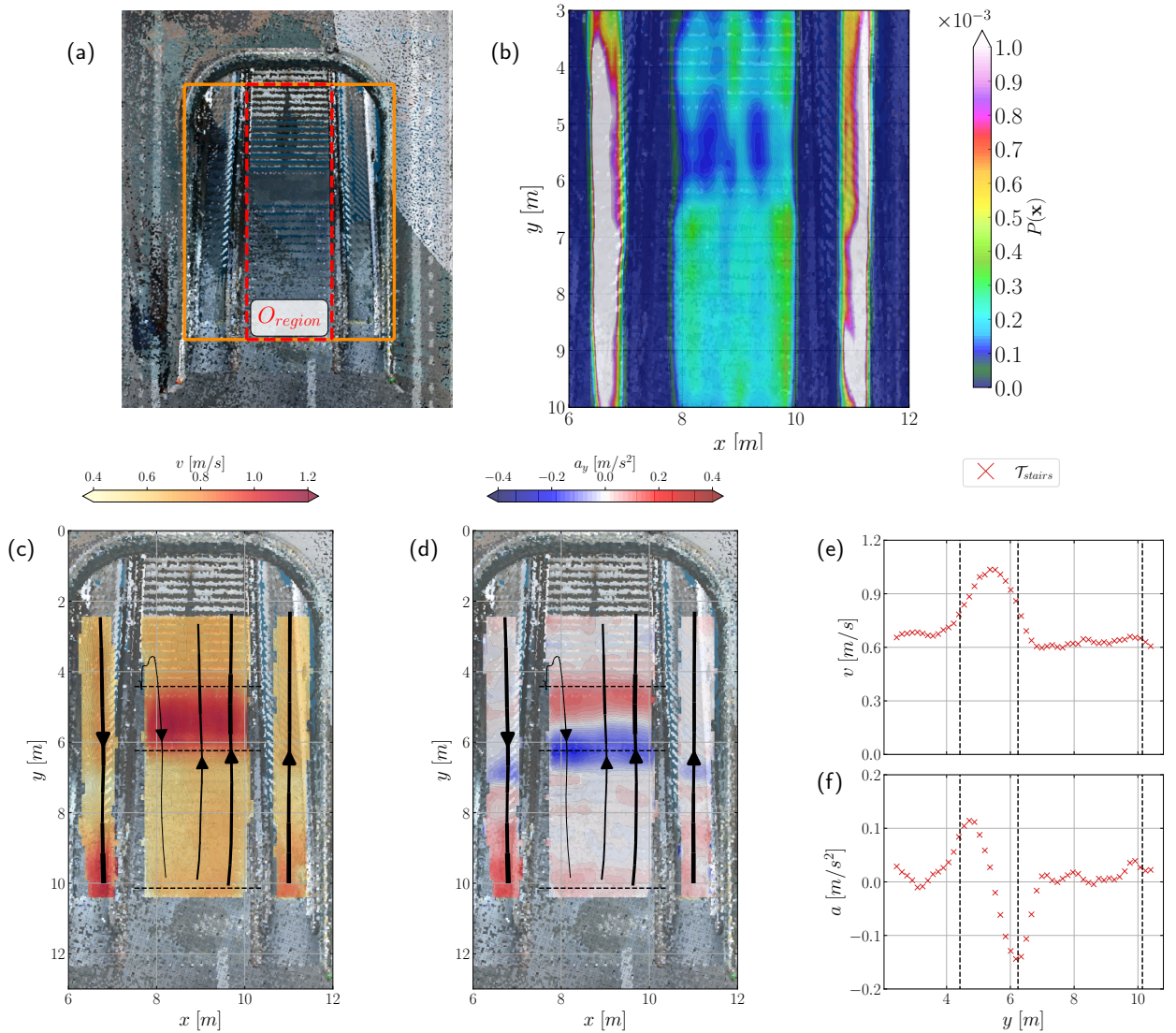


**Figure 5:** (a) Overhead image of the staircase considered. Our sensors covered area within the orange rectangle. We consider here the staircase region  $O_{region}$  bounded by the dashed red line. (b) Probability distribution function of pedestrian position represented as a heatmap. We observe three walking lanes across the staircase. (c, d) The distributions of velocity and acceleration across the staircase-escalator system. We observe a higher walking velocity on the flat staircase landing. Both images are imposed with flow vectors indicating the direction of the flow. We observe that pedestrians walk on the right side of the staircase following the direction of the escalators. (e, f) Cross-sections of the velocity (e) and acceleration (f) on the staircase. All distributions are computed by considering the entire dataset  $\mathcal{T}$ .

position (e.g. Steffen and Seyfried (2010)), enabling a local definition of the density field as the reciprocal of the local Voronoi cell area. This method provides robust, although computationally expensive, density estimates in the bulk of the flow and at sufficiently high density levels. On the other hand, in the absence of neighboring pedestrians, the Voronoi cells result unbounded with local density degenerating to zero. This issue can be mitigated by limiting the size of the cells to the boundaries of the observed geometry (hence all cells result closed) and/or by thresholding each cell (to prevent density underestimation).

In order to deal efficiently with high statistics data and prevent unbounded cells, we consider here an approach that builds on bounding individual areas from the start, echoing the concept of personal space. The personal space is defined as the space a walking pedestrian tries to maintain around the body. While it is understood to be elliptical (axes:

2 m in longitudinal and 0.5 m in lateral direction according to G erin-Lajoie, Richards, Fung and McFadyen (2008)), we approximate the individual personal space of the pedestrian,  $i$ , as a circular region with radius  $R = 0.75$  m and area  $\pi R^2 = 1.86$  m<sup>2</sup>. In level-of-service terms, this is at the interface between level A (free-flow) and B (slightly restricted flow), as defined by Fruin (1971). We compute the instantaneous density as the ratio between the number of observed pedestrians and the union of all the personal spaces,

$$\hat{S}_{stairs} = \text{Area} \left( \bigcup_{i=1}^N S_i \cap O_{region} \right) \leq \text{Area}(O_{region}) = \bar{S} \approx 25 \text{ m}^2, \quad (8)$$

i.e.

$$\hat{\rho} = \frac{N}{\hat{S}_{stairs}}, \quad (9)$$

where  $O_{region}$  indicates the observation region, that is used as outer limit of the personal areas. Note that according to Eq. (9), the density has the following lower and upper bounds:

$$\max \left\{ \frac{1}{\pi \cdot R^2}, \frac{N}{\bar{S}} \right\} \leq \hat{\rho} \leq \frac{N}{\pi \cdot R^2}. \quad (10)$$

The lower bound entails the maximum between two components. The constant  $1/(\pi R^2) = 0.56$  m<sup>2</sup> is attained when personal spaces do not overlap. Moreover, due to  $\hat{S}_{stairs} \leq \bar{S}$  (Eq. (8)), our density definition is always larger than the hydrodynamic definition (Eq. (7)), that for small  $N$  can get arbitrarily close to zero; see also Appendix B). The density value  $\hat{\rho}$  increases as personal spaces overlap (mutual distances  $d < 2 \cdot R$ ), reducing the union in Eq. (8). This yields a theoretical upper bound corresponding to the case in which all the personal areas perfectly overlap. This is clearly a non-physical upper bound due to necessary volume exclusions. More realistically, for the case of  $N$  very large, personal areas will fill the available surface  $O_{region}$ . This assumption enables to provide a more realistic asymptotic behavior to  $\hat{\rho}$ , which approaches the hydrodynamic density (see also trends in Fig. 15(b)).

### 3. Results

#### 3.1. Average dynamics: pedestrian flux and free-stream velocity

We start our analysis by providing an overview of the overall usage of the stairs-escalator system in terms of typical daily fluxes, fluxes distribution, directionality and velocities.

*Flux and flow partition.* In Fig. 4a we provide an example of pedestrian fluxes recorded during a typical working day (2022-04-12), for the four different subset of trajectories ( $\mathcal{T}_{stairs\uparrow}$ ,  $\mathcal{T}_{stairs\downarrow}$ ,  $\mathcal{T}_{esc\uparrow}$ ,  $\mathcal{T}_{esc\downarrow}$ ) previously defined in Sec. 2. We observe high fluxes during rush hours, with average peaks of 50 ped/m in the morning (7 am - 9 am) where the majority of commuters descend from the platform to the train station (blue and green curves), and in the afternoon (16 pm - 18 pm) where flows in the opposite direction (orange and red curves) play a more relevant role, with average peaks of 20 ped/m. We shall remark that the asymmetry between morning and afternoon is specific to the train platform considered in our study, and is due to the train schedule.

In Fig. 4b we show aggregated flux statistics, in terms of pedestrians per hour, for each one of the trajectory subsets. The data highlights a strong preference towards the usage of the escalator. The average flux for  $\mathcal{T}_{esc\uparrow}$  ( $\mathcal{T}_{esc\downarrow}$ ) is 276 ped/h (180 ped/h), while for the staircase we report 46 ped/h and 131 ped/h, respectively for  $\mathcal{T}_{stairs\uparrow}$  and  $\mathcal{T}_{stairs\downarrow}$ . The overall fraction of people choosing the escalator over the staircase is 0.72, which becomes 0.86 when considering only the subset of people going upstairs, and 0.58 when considering only people going downstairs.

While the staircase is prominently used in downstairs direction, bidirectional flows also occur. In Fig. 4d we report the probability distribution of the flow compositions as a function of the pedestrian occupation on the stairs. We consider 5 categories with different direction ratios, respectively: 1,2) unidirectional flow i.e. pedestrians all move downstairs 100%  $\mathcal{T}_{stairs\downarrow}$  or all pedestrians move upstairs 100%  $\mathcal{T}_{stairs\uparrow}$ ; 3) balanced bidirectional [40 – 60]%  $\mathcal{T}_{stairs\uparrow\downarrow}$ , i.e. an almost equal number of people are simultaneously going upstairs and downstairs; 4,5) unbalanced bidirectional flow, i.e. the majority of pedestrians is going downstairs [60 – 99]%  $\mathcal{T}_{stairs\downarrow}$  or the majority of pedestrians is going upstairs [60 – 99]%  $\mathcal{T}_{stairs\uparrow}$ . We rarely observe a balanced bidirectional flow, especially for high crowd densities. Considering the primarily unidirectional flow, the aforementioned asymmetry between morning and afternoon does not influence our study.

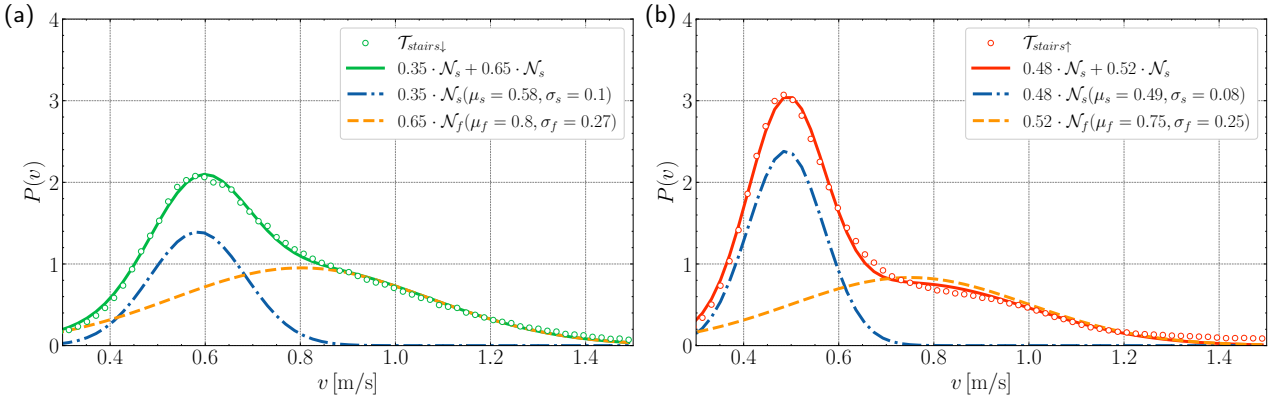


**Figure 6:** Probability distribution of the free-stream walking velocity for (a) downstairs and (b) upstairs motion. We fit a mixture of two Gaussian distributions (Eq. (11)) representing the slow (blue dash-dotted line) and fast (yellow dashed line) walking dynamics.

*Free-stream velocity.* We now take into consideration the free-stream dynamic, i.e. we consider configurations in which only one pedestrian at a time moves on the staircase in either direction. The average walking speed in upstream direction is  $\langle v \rangle_{stairs\uparrow} \approx 0.63$  m/s, with  $\langle v \rangle_{stairs\downarrow} \approx 0.73$  m/s for the downstream direction. The observed 0.1 m/s speed difference between ascending and descending well compares with the 10% difference in speed reported by Fruin (1971), and with previous figures from literature (Table. 1). However, thanks to the vast collection of trajectories gathered during our tracking campaign, in this work we can take our analysis beyond the average case. In Fig. 4c we report the probability distributions of the free-stream velocity. The red curve represents the case  $\mathcal{T}_{stairs\uparrow}$ , while the green one the case  $\mathcal{T}_{stairs\downarrow}$ . For comparison, we also present a distribution of the walking speed on the train platform (brown curve), which was obtained from pedestrian trajectories measured by a commercial pedestrian tracking setup installed in front of the staircase - similar to the setup used in Pouw, Toschi, van Schadewijk and Corbetta (2020); Pouw et al. (2022). The walking speed on the staircase exhibits a skewed distribution, with a pronounced right tail, representing cases of fast walking/running people. As a result, average speed values are significantly higher than the modal ones, with respectively  $\text{mode}(v)_{stairs\uparrow} \approx 0.48$  m/s and  $\text{mode}(v)_{stairs\downarrow} \approx 0.58$  m/s for ascending and descending. On the platform, we observe the opposite behavior, with a left-tailed distribution, where due to pedestrian waiting for their train the modal value ( $\text{mode}(v)_{platform} \approx 1.23$  m/s) is significantly higher than the average ( $\langle v \rangle_{platform} \approx 1.02$  m/s). In order to quantify the ratio between slow and fast walkers, we take into consideration a Gaussian-mixture modeling for the probability distribution of the free-stream velocity for the different cases presented in Fig. 4c. This modeling approach is aligned with the findings of Saberri, Aghabayk and Sobhani (2015) which demonstrated that a mixture of two Gaussian distributions provides a robust fit for pedestrian bidirectional velocity data. In order to allow for a simple physical interpretation, we consider a 2-component model:

$$P(v) \sim \phi_s \mathcal{N}(\mu_s, \sigma_s) + \phi_f \mathcal{N}(\mu_f, \sigma_f), \quad \phi_s + \phi_f = 1, \quad (11)$$

where  $\mathcal{N}$  is a Gaussian distribution with mean  $\mu_i$ , variance  $\sigma_i$  and weight  $\phi_i$ , and where the subscript  $s$  (or  $f$ ) is used to refer to the parameters for slow (or fast) walkers. In Fig. 6 we show the fit for the data shown in Fig. 4c using Eq. (11). For the descending case we fit a Gaussian-mixture model with parameters  $P(\phi_s = 0.35, \mu_s = 0.58, \sigma_s = 0.1, \phi_f = 0.65, \mu_f = 0.8, \sigma_f = 0.27)$ . For the ascending case, instead, the results of the fit yields  $\phi_s = 0.48, \mu_s = 0.49$  m/s,  $\sigma_s = 0.08$  m/s,  $\phi_f = 0.52, \mu_f = 0.75$  m/s,  $\sigma_f = 0.25$  m/s.

*Eulerian Fields.* The stairs-escalator system has relatively narrow side boundaries (about 5 body diameters). In combination with the intermediate landing, this yields dynamics that are not spatially uniform. We consider this in terms of floor usage and of walking velocity field. As pedestrians ascend or descend the stairs, and as they traverse the landing, they adjust their speed accelerating and decelerating. Here, we report Eulerian fields of space occupancy (position probability distribution), average speed, and acceleration, computed on the entire dataset  $\mathcal{T}$ .

In Fig. 5b, we report the probability distribution of pedestrian positions,  $\mathbb{P}(\mathbf{x})$  (colormap: probability iso-contour). Consistently with Fig. 4b, the escalators area feature the highest occupancy probability, peaking on the ascending

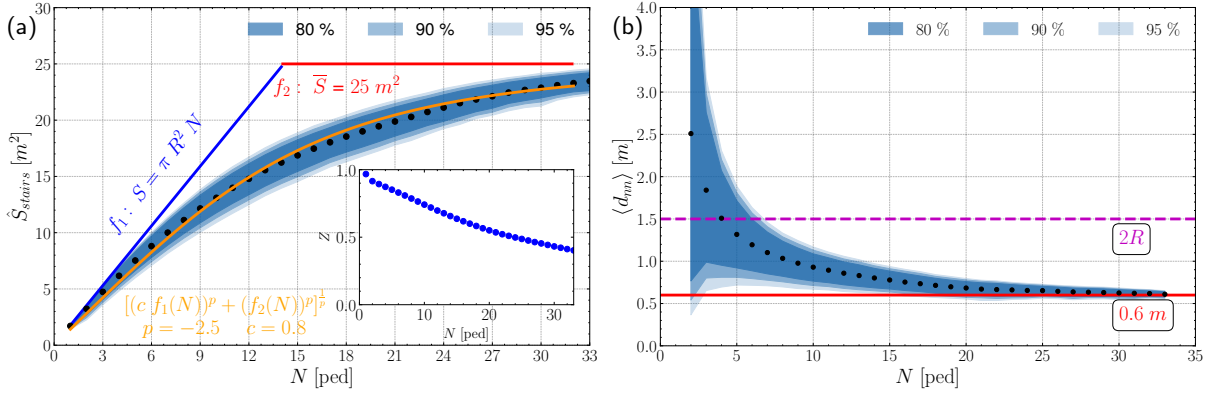


**Figure 7:** (a) Personal space union,  $\hat{S}_{stairs}$ , as a function of the number of pedestrians on the staircase. The average is represented with black dots and we show the 80<sup>th</sup>, 90<sup>th</sup>, and 95<sup>th</sup> percentiles with different shades of blue. This provides insight in how the area is filled, with pedestrians accepting to occupy less than the available space, allowing for a compression. We superimpose the theoretical bounds to the occupied area, respectively  $f_1(N) = \pi R^2 N$  (blue line; all individual spaces do not intersect and are sufficiently far from the boundary) and the area of the staircase  $f_2(N) = \bar{S} \approx 25 \text{ m}^2$  (red line). While having initially a linear trend,  $\hat{S}_{stairs}$  departs immediately from  $f_1(N)$  and, for large  $N$ , the area approaches the global area. We report in yellow our model  $\hat{S}_{stairs}^{model}(N)$  (Eq. (15)), that through the single parameter  $p = -2.5$  models the willingness of people of using less the space than available. In this respect, in the inset we report the compressibility factor  $Z$  (Eq. (14)) (b) Frame averaged mutual distance between closest neighbors  $\langle d_{nn} \rangle$  as a function of the stairs occupation  $N$ . We observe a decrease in the mutual distance as the area gets filled with more pedestrians, converging to a minimal frame averaged mutual distance  $d_{nn} \approx 0.6 \text{ m}$ .

escalator. A clear lane on the right-hand side of each escalator is observable. This is generated by pedestrians standing on escalators on the right while leaving the left side to people that overtake.

In the bulk of the staircase area, trajectories align along three main lanes. These lanes are especially pronounced along the ascending/descending region, while they are dimmer in the landing area. This can be explained considering the average walking speed field (Fig. 5c), The average in  $x$  direction of the speed field is reported as a function of  $y$  in Fig. 5e). We observe that the average speed on the staircase is around 0.6 m/s, but in the landing zone it increases up to 1 m/s. This velocity growth renders the average permanence time on the landing smaller thus the lower probability. In Fig. 5d, we report the field of acceleration in  $y$  direction,  $a_y$  (transversal average in Fig. 5e). Consistently with the speed field, we observe a strong acceleration about half meter before the landing and, symmetrically, a deceleration that starts almost immediately after the person sets foot on the landing. Finally, a net increase in velocity is observable at the end of the ascending escalator, as people start to walk when they are close to the surface.

### 3.2. Density patterns and interpersonal distance: crowd compressibility

In the previous section, we have highlighted the heterogeneous composition of flow patters from data, showing how throughout the day one can observe high density clusters alternating with low density to free-stream configurations. We discuss here how density effectively scales with the number of observed pedestrians and, as such, how the available area is filled.

In Fig. 7a we report the size of the occupied area (Eq. (8)) as a function of the number of pedestrians. This shows how the surface area on the staircase gets filled due to how pedestrians choose to position themselves (see also examples in Fig. 8). The area  $\hat{S}_{stairs}$  is formed by the union of personal space spheres from single individuals. Therefore,  $\hat{S}_{stairs}$  admits an upper bound given by the maximum between  $N$  disjoint personal space spheres (scaling as  $\pi R^2 N$ , blue line in Fig. 7a), and the total (horizontal) surface of the area of interest ( $\bar{S} = \text{Area}(O_{region}) \approx 25 \text{ m}^2$ , red line in Fig. 7a). In formulas this reads

$$\left\{ \begin{array}{l} \hat{S}_{stairs}(N) \leq \hat{S}_{stairs}^{\max}(N) = \min\{f_1(N), f_2(N)\} \\ f_1(N) = \pi R^2 N \\ f_2(N) = \bar{S} \end{array} \right. \quad (12)$$

In Fig. 7a, we report the average observed value of  $\hat{S}_{stairs}(N)$ ,  $\langle \hat{S}_{stairs} \rangle(N)$ , and some percentiles. The average occupied area  $\langle \hat{S}_{stairs} \rangle(N)$  grows linearly at small  $N$  ( $N < 6$ ), yet with a smaller slope than the upper bound: Eq. (12)

$$\langle \hat{S}_{stairs} \rangle(N) \approx c f_1(N) \quad c \approx 0.8, \quad N < 6. \quad (13)$$

The constant  $c < 1$  is a consequence of multiple potential factors: on one hand, we expect people to not strictly maintain a distance  $d > 2R$  even at small density - thus, yielding overlapping personal spaces. This can be due, e.g., to small social groups, whose individuals opt to walk in close proximity (see, e.g., Zanlungo et al. (2014)); note that in a similar Dutch train station we measured about 15%-20% of the people to be in a group Pouw et al. (2020)). Secondly, the definition itself of the personal radius,  $R$ , has some degree of arbitrariness. As  $N$  grows, the occupied area smoothly approaches the available surface. Thirdly, our definition of occupied area is bounded by the observation region  $O_{region}$ . This means that pedestrians close to the boundaries experience a personal area smaller than the limit  $\pi R^2$ . Later in the section, considering the dependencies on mutual distances, we shall partially disentangle the roles of these factors.

The key observation here is that people willingly accept to occupy less than full available area, accepting a ‘‘compression’’. Occupying the full area available would mean having  $\hat{S}_{stairs}(N)$  growing linearly at small  $N$  (accounting for possible arbitrariness in  $R$ ), up to the saturation at  $\bar{S}$  that is reached with a kink point. Note that this happens even though in diluted crowds pedestrians are free to reposition themselves and, for instance, are able to overtake slower walking pedestrians.

Conversely, the average (as well as high percentiles) of the occupied area depart rapidly from the theoretical bound and from a linear growth. We quantify this in terms of compressibility factor (see, e.g., for the definition of compressibility factor for gasses Zucker and Biblarz (2019))

$$Z = \frac{\hat{S}_{stairs}}{f_1(N)}, \quad (14)$$

i.e. the ratio between the occupied area and the maximum  $f_1(N)$  assuming no overall geometric boundaries (inset in Fig. 7a). The observed compressibility factor rapidly decreases from 1 as to indicate the presence of attractive interactions, which lower the area usage.

We further model this compressibility effect in terms of a power  $p < 0$  of the  $p$ -norm between the two functions  $c f_1(N)$  and  $f_2(N)$ :

$$\hat{S}_{stairs}^{model}(N) = \left[ (c f_1(N))^p + f_2(N)^p \right]^{\frac{1}{p}}. \quad (15)$$

Note that Eq. (15), in the limit  $p \rightarrow -\infty$ , converges to the theoretical bound (i.e. a linear trend connected with a kink to the saturated capacity, Eq. (12) - this is a well known property of  $p$ -norms). As  $p$  grows from  $-\infty$ , the transition between  $c f_1$  and  $f_2$  becomes increasingly smoother (e.g.  $p = -1$  yields their harmonic mean). Considering  $c \approx 0.8$  (cf. Eq. (13)), we found  $p = -2.5$ . We stress that this  $p$  number encodes for a non-trivial crowd dynamics effect, specifically the willingness of pedestrians to accept a compression. We expect that the  $p$ -value will in principle depend on cultural differences, habits, geometry and crowd flow conditions.

We conclude the section by considering the dynamics from the perspective of single individuals analyzing how pedestrians arrange in space and how this influences the dynamics. Our key parameter is the average distance to the nearest neighbor. Specifically, for every pedestrian,  $i$ , we measure on a frame-by-frame basis the distance to their closest peer  $j$ :

$$d_{i,m} = \min_j \{ |\mathbf{x}_i - \mathbf{x}_j| \}. \quad (16)$$

We then retain the frame-by-frame averages values of  $d_{i,m}$ :

$$\langle d_{nn} \rangle = \frac{1}{N_{frame}} \sum_{i=1}^{N_{frame}} d_{i,m}. \quad (17)$$

In Fig. 7b, we report the frame-averaged distance  $\langle d_{nn} \rangle$  as a function of stairs occupation  $N$ . For  $N \leq 3$  the average nearest neighbor distance remains well above  $2R$  with, however, large fluctuations. This supports the presence of

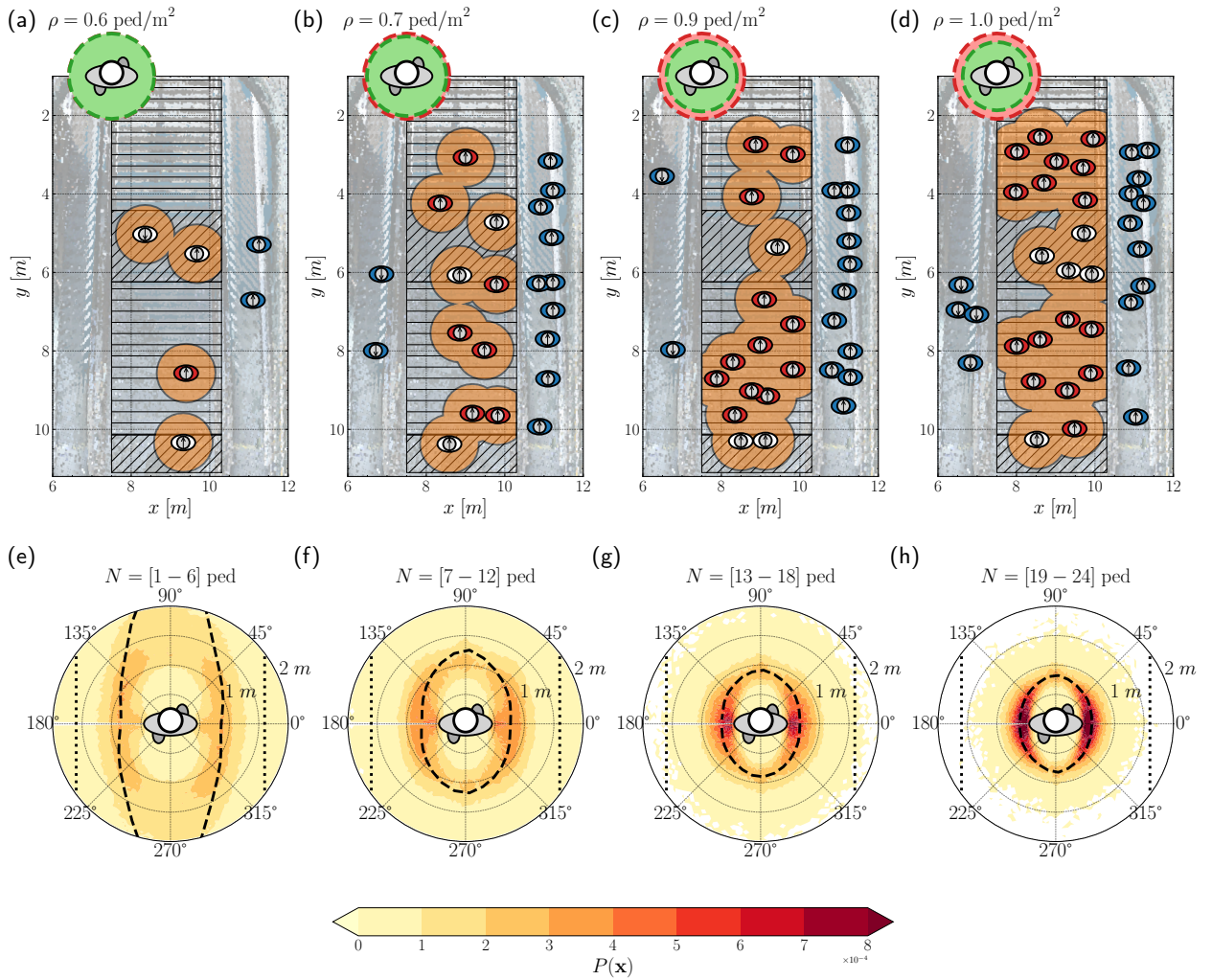


**Figure 8:** (a-d) Overhead images of the staircase showing examples of the four increasing levels of stair occupation with respectively 4, 10, 15, and 21 pedestrians. Pedestrians located on the inclined plane of the staircase are colored in red, pedestrians located on a flat part of the staircase in white, and pedestrians on the escalators in blue. We indicate the occupied area from Eq. (8) with an orange color. On top of each panel we show the pedestrian density as calculated using Eq. (9). (e-h) Spatial probability distribution of nearest neighbor positions for the four increasing levels of stair occupation. We split our data set based on the stairs occupation in four evenly-sized bins with sides at  $N = \{1, 7, 13, 19, 25\}$  pedestrians. A red color indicates high probability and a yellow color low probability. We report the average distance to nearest neighbors in a certain direction using a black dashed line. We observe an elliptical shape for low crowd density i.e. people allow others to be close in lateral direction but not in longitudinal direction. As the crowd density increases the shape becomes more circular and the radius decreases. To provide a sense of scale we impose two dotted black lines separated by  $w = 3.2 \text{ m}$ , indicating the width of the staircase. Additionally, we impose an ellipse to indicate the typical body size.

social groups ( $\langle d_{nn} \rangle \approx R$ ), but also the fact that pedestrians opt to walk close to boundaries even at low densities (in fact this yields a reduction  $\hat{S}_{stairs}$  from the upper bound  $f_1(N)$  due to the fact that only personal areas within  $O_{region}$  are considered). On the other hand, as the density increases, the average distance approaches a limiting value  $\langle d_{nn} \rangle \approx 0.6 \text{ m}$ . Note that two threads of the staircase measure  $0.6 \text{ m}$ .

We conclude the section by considering how nearest neighbors arrange in space and how this affects the dynamics. For each pedestrian  $i$ , we measure frame-by-frame the relative position of the nearest neighbor. In Fig. 8, we present heatmaps of the spatial distribution for the location of nearest neighbors for increasingly large values of the local density. In diluted conditions we observe low probabilities for finding the nearest neighbor aligned with the direction

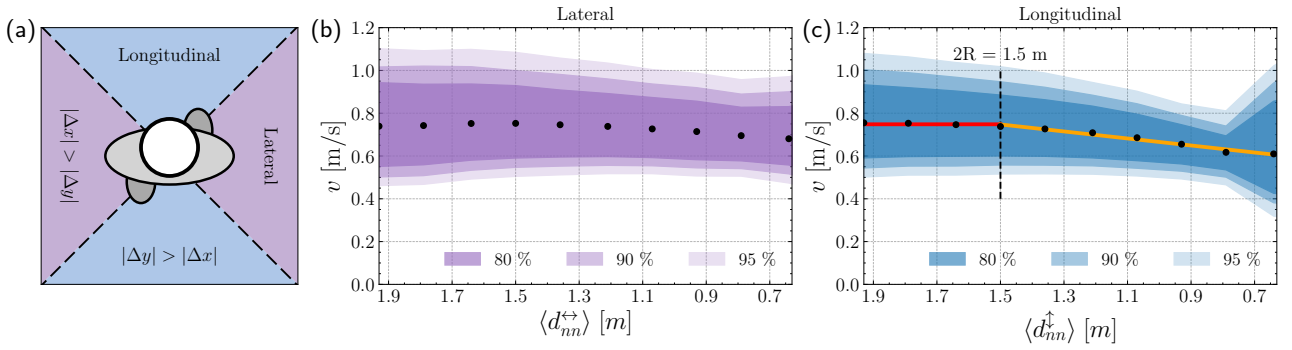


**Figure 9:** (a) We consider a nearest neighbor to be positioned on the side if the transversal distance between the considered pedestrian and the neighbor is larger than the longitudinal direction ( $|\Delta x_{ij}| > |\Delta y_{ij}|$ , purple region). We consider a pedestrian in the front/back otherwise ( $|\Delta x_{ij}| < |\Delta y_{ij}|$ , blue region). (b,c) Walking velocity,  $v$ , as a function of the frame averaged distance between closest neighbors restricting to a closest neighbor in transversal direction (b) and longitudinal direction (c). In (c) we fit for  $\langle d_{nn} \rangle > 1.5$  m a constant,  $v(\langle d_{nn} \rangle) = 0.75$  m/s, with a red line and for  $\langle d_{nn} \rangle < 1.5$  m a linear fit otherwise (orange line, cf. Eq. (19)). We observe from (b) that a high lateral density does not impact the flow velocity and from (c) that the flow velocity decreases as the longitudinal distance between pedestrians gets less than  $\langle d_{nn} \rangle = 1.5$  m. The velocity fluctuations decrease until  $\langle d_{nn} \rangle \approx 0.8$  m, for smaller closest neighbor distances (typically higher density) the fluctuation increase again. This likely connects with the necessity of avoidance/overtake maneuvers.

of traveling. On the other hand the probability is maximum along the lateral direction, for a distance  $d \approx 0.9$  m. In the Figure we report with a black dotted line the iso-contour given by the most probable value  $\langle d_{nn} \rangle \approx 0.6$  m.

In Fig. 8(bottom panels), we present heatmaps of the spatial distribution for the location of nearest neighbors for increasingly large values of the local density (examples of pedestrians distribution at the related density values are in the top panes). We report with a black dotted line the 1d-manifold given by the most probable location of nearest neighbors in every direction. This yields an elliptical shape, with major axis aligned along the pedestrian walking direction, but with decreasing eccentricity as the local density is increased. In diluted conditions, we observe that closest neighbors have maximum probability to be located along the sides ( $d_{side} \approx 0.9$  m), conversely plenty of headway ( $d_{headway} > 2.5$  m) is left in frontal direction. As density increases the manifold of the average nearest neighbor position contracts approaching the  $d \approx 0.6$  m, consistently with the asymptotic trend of Fig. 7.

As one can expect (e.g., Subaih, Maree, Tordeux and Chraïbi (2022)), the position of the closest neighbor influences pedestrians in an anisotropic way. To conclude the section, in Fig. 9, we report the frame-averaged walking velocity (Eq. (4)) as a function of the average distance between nearest neighbors (Eq. (17)). Note that here we make no distinction between pedestrians ascending and descending the stairs. We separate the condition in which the nearest neighbor is positioned on the side ( $|\Delta x_{ij}| > |\Delta y_{ij}|$ , cf. Fig. 9a), and in the front/back ( $|\Delta x_{ij}| < |\Delta y_{ij}|$ ). To avoid confusion, we indicate these distances as  $\langle d_{nn}^{\leftrightarrow} \rangle$  and  $\langle d_{nn}^{\downarrow} \rangle$ , and report the velocity in dependence on these quantities respectively in Fig. 9b and 9c. From Fig. 9b, we observe that a closest neighbor on the lateral side has practically no influence on the average velocity, i.e.

$$v(\langle d_{nn}^{\leftrightarrow} \rangle) \approx 0.75 \text{ m/s} \quad \forall \langle d_{nn}^{\leftrightarrow} \rangle. \quad (18)$$

Conversely,  $v$  shows strong variations when the closest neighbor approaches in longitudinal direction reducing the headway (Fig. 9c). In particular, the velocity 0.75 m/s (cf. Eq. (18)) holds only for  $\langle d_{nn}^{\downarrow} \rangle < 1.5$  m, and decreases otherwise. Overall, we observe the following piece-wise approximated dependency

$$v(\langle d_{nn}^{\downarrow} \rangle) \approx \begin{cases} 0.75 \text{ m/s} & \langle d_{nn}^{\downarrow} \rangle > 1.5 \text{ m} \approx 2R \\ 0.16 \cdot \langle d_{nn}^{\downarrow} \rangle + 0.5 & \langle d_{nn}^{\downarrow} \rangle < 1.5 \text{ m} \end{cases} \quad (19)$$

Units  $v$  : [m/s]  $\langle d_{nn}^{\downarrow} \rangle$  : [m].

Notice that the transition around  $1.5 \text{ m} \approx 2R$  supports our scale for the definition of the size of the personal space (Sec. 2.3).

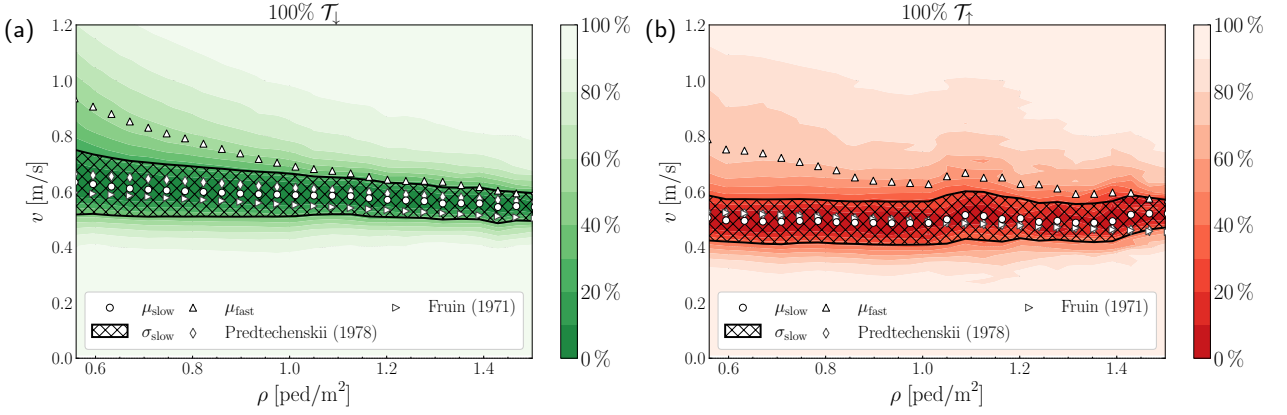


**Figure 10:** Fundamental diagrams for (a) unidirectional flow descending,  $100\% \mathcal{T}_\downarrow$ , and (b) unidirectional flow ascending,  $100\% \mathcal{T}_\uparrow$  reporting the walking velocity as a function of the crowd density. We use a colormap to show the confidence intervals in our data set. We include the average walking speed of slow walkers  $\mu_{slow}$  (circles) with a hatched domain to show one standard deviation to the mean of slow walkers  $\sigma_{slow}$ . Additionally, we report the average walking speed of fast walkers  $\mu_{fast}$  (upward pointing triangles), and for comparison the FD reported by Fruin (1971) (right pointing triangles) and by Predtechenskii and Milinskii (1978) (diamonds).

In Fig. 9b, we further notice that the velocity fluctuation decreases until  $\langle d_{nn}^\downarrow \rangle \approx 0.8$  m, to then increase substantially. This likely connects with the fact that as the pedestrian in front gets too close, evasive maneuvers become necessary.

### 3.3. Probabilistic fundamental diagrams

In this section, we employ our trajectory dataset to report and compare fundamental diagrams (FD) (density-velocity relations) for pedestrians ascending and descending our staircase. We specifically consider probabilistic counterparts of fundamental diagrams, that include average (and modal) velocities, common fluctuations (fractions of one standard deviation), and rare fluctuations (percentiles of the speed distributions conditioned to the density). It is clear that only very high statistics datasets can serve to this purpose. In Fig. 10 we present the fundamental diagram for the walking velocity, as function of the pedestrian density on the staircase. We restrict our analysis to unidirectional flows, showing in panel (a) the case where all pedestrians descend the staircase, with the ascending case shown in panel (b). In each plot, we show with a colormap the confidence intervals of our data for given densities i.e. the percentage of recordings at that density that falls within the interval. For comparison, we also include in the plot the FD by Fruin (1971) and Predtechenskii and Milinskii (1978), which can be parametrized with the following expressions (from Chen et al. (2018))

$$v(\rho)_{\text{fruin}} = -0.097 \cdot \rho + 0.65, \quad v(\rho)_{\text{predtechenskii}} = 0.009 \cdot \rho^2 - 0.125 \cdot \rho + 0.73 \quad (20)$$

$$\text{Units } \rho : [\text{ped}/\text{m}^2] \quad v : [\text{m}/\text{s}]$$

for the descending case, and

$$v(\rho)_{\text{fruin}} = -0.077 \cdot \rho + 0.57, \quad v(\rho)_{\text{predtechenskii}} = 0.003 \cdot \rho^2 - 0.08 \cdot \rho + 0.57 \quad (21)$$

$$\text{Units } \rho : [\text{ped}/\text{m}^2] \quad v : [\text{m}/\text{s}]$$

for the ascending case.

Finally, we report in the diagram the average values of the parametrization of the velocity distribution function (for a fixed density value), which was established in Eq. (11), and which allows to treating the average walking speed of slow and fast walkers separately.

From Fig. 10a, we observe that average walking speed of slow walkers  $\mu_{slow}$  falls in between the two curves in Eq. (20), taking an average value of  $\approx 0.6$  m/s, almost independent with respect to the local density. On the other hand, for fast walkers ( $\mu_{fast}$ ), we observe a significant decreasing trend, starting from a free-flow value of  $\approx 1.0$  m/s which

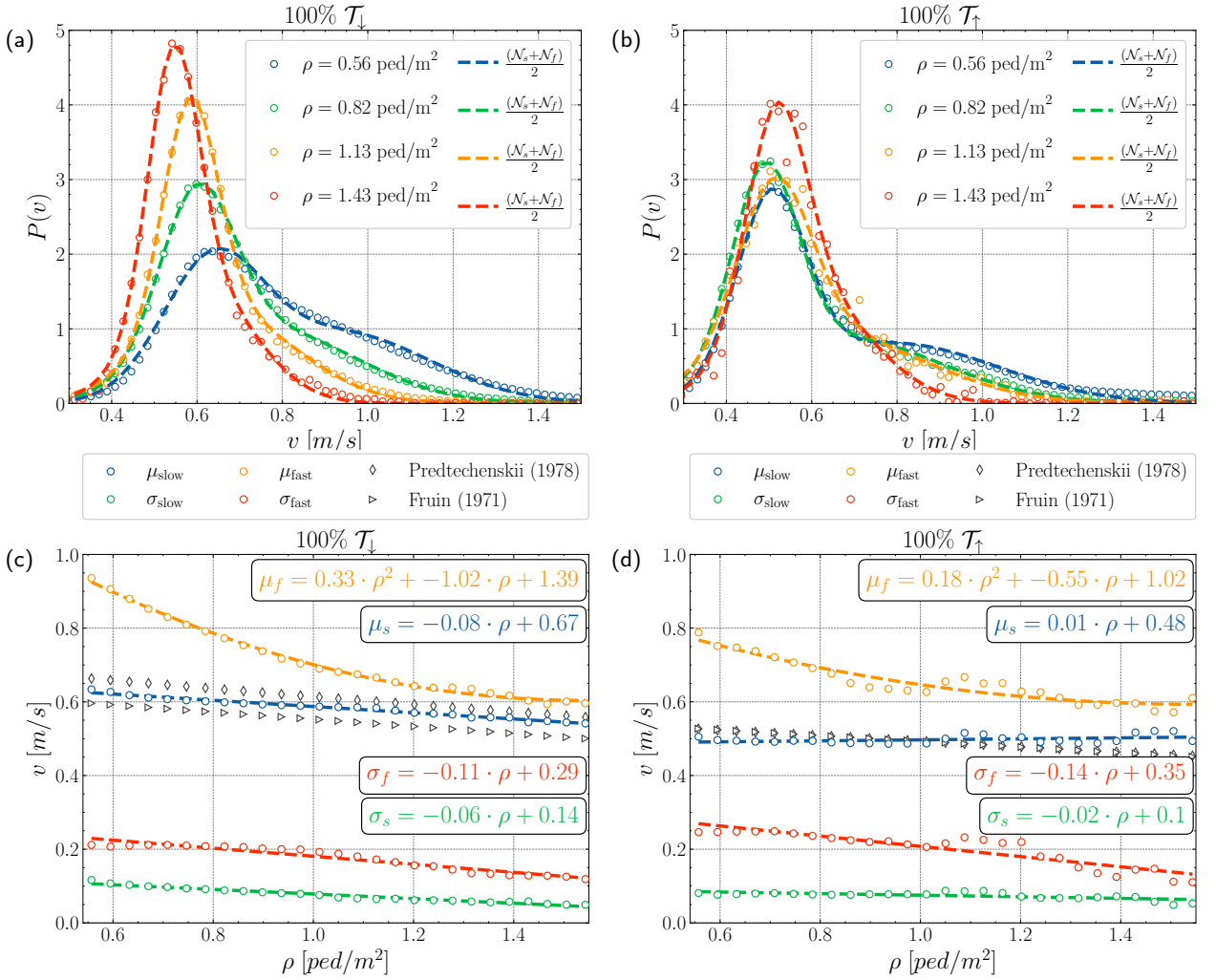


**Figure 11:** (a,b) Probability distribution function of the walking velocity on the staircase at crowd densities  $\rho = [0.56, 0.82, 1.13, 1.43]$  ped/m<sup>2</sup> for (a) descending and (b) ascending pedestrian movement. Every distribution is fitted with a Gaussian mixture with equal weights (Eq. (22)). (c,d) the Gaussian mixture fit parameters  $\mu$  and  $\sigma$  across the observed density range for the slow and fast (c) downstairs and (d) upstairs walking movements. We employ a linear fit to  $\mu_{slow}$ ,  $\sigma_{slow}$  and  $\sigma_{fast}$  and a quadratic fit to  $\mu_{fast}$ . We include the fundamental diagram by Fruin (1971) and Predtechenskii and Milinskii (1978) (Eq.(20) and Eq.(21)) for comparison.

converges to  $\mu_{slow}$  for larger values of the local density (i.e. in this case we cannot really distinguish fast and slow walkers). This pattern emerges also looking at fluctuations around the mean, which decrease at large density values, as shown by the colormap.

Similar considerations apply to Fig. 10b, where we consider, instead, the case of pedestrians walking in ascending direction. Here, the difference between slow and fast walkers is more pronounced at large density values, although fewer data is available in this case (see Fig. 4d).

We conclude by providing a compact parametrization of the data presented in Fig. 10, to aid future comparisons, and especially, to allow using the information reported here in realistic simulations of pedestrian flows on staircases. We consider once again Eq. (11), this time for simplicity we use equal weights for the Gaussian distribution associated to slow and fast walkers, i.e.:

$$P(v) \sim \frac{1}{2} \left( \mathcal{N}(\mu_s, \sigma_s) + \mathcal{N}(\mu_f, \sigma_f) \right) \quad . \quad (22)$$

Next, we use Eq. (22) to fit the (empirical) distribution function of pedestrian walking velocity for fixed values of density. We report a few examples in Fig. 11a and Fig. 11b, for flows in descending and ascending direction respectively, which show that the approximation  $\phi_s = \phi_f = 1/2$  allows for an excellent fit of the PDFs. We conclude taking a further step, which consists in fitting the parameters of the two Gaussian distributions as function of the local density  $\rho$ . The results of the fit, reported in Fig. 11c-d, delivers the following expressions:

$$\begin{aligned} \mu_f &= 0.33\rho^2 - 1.02\rho + 1.39, & \sigma_f &= -0.11\rho + 0.29 \\ \mu_s &= -0.08\rho + 0.67, & \sigma_s &= -0.06\rho + 0.14 \end{aligned} \quad (23)$$

$$\text{Units } \rho : [\text{ped/m}^2] \quad \mu_{s/f} : [\text{m/s}] \quad \sigma_{s/f} : [\text{m/s}]$$

for the descending case, and

$$\begin{aligned} \mu_f &= 0.18\rho^2 - 0.55\rho + 1.02, & \sigma_f &= -0.14\rho + 0.35 \\ \mu_s &= 0.01\rho + 0.48, & \sigma_s &= -0.02\rho + 0.10 \end{aligned} \quad (24)$$

$$\text{Units } \rho : [\text{ped/m}^2] \quad \mu_{s/f} : [\text{m/s}] \quad \sigma_{s/f} : [\text{m/s}]$$

for the ascending case.

## 4. Discussion

In this work, we investigated with unprecedented statistical resolution the dynamics of pedestrians as they ascend or descend a large staircase in a railroad station (Eindhoven Central Station, The Netherlands). By employing a state-of-the-art pedestrian tracking system based on a grid of overhead depth sensors and hinging on the latest computer vision algorithms, we have recorded over 3 million individual trajectories under various flow conditions (unidirectional and bi-directional with various level of mixing), in an unbiased and privacy-respectful manner. The dataset that we collected is at least three orders of magnitude larger in terms of data volume than datasets currently considered in the literature. This is key in order to study pedestrian dynamics beyond the averages in terms of fluctuations. Our experimental dataset is characterized by extremely high accuracy, with an F1 Score on localization always above 96% and above 99% for less than 0.95 ped/m<sup>2</sup>, thanks to a dedicated hand-annotated training set and effective data augmentation. Due to its real-life nature the dataset is limited to crowd densities not exceeding 1.5 ped/m<sup>2</sup>.

We provided a phenomenological analysis of pedestrian dynamics considering various key components. First, we investigated spatial fields of positions, velocity and accelerations. For a staircase as ours, pedestrians would arrange with the highest probability along three parallel lanes. These lanes, partially diffuse on the intermediate landing due to speed changes. The velocity and acceleration fields show that the walking velocity is non-uniform on the staircase. In free flow, we observed velocities, on average, of 0.63 m/s in ascending direction and 0.73 m/s while descending. These readings have an increment larger than 50% (reaching 1.1 m/s) when people step on the intermediate landing. The walking velocity on the landing remains however significantly lower than what observed on the rest of the platform (mode: 1.23 m/s). This is likely due to the short length of the landing (1.5 m) that does not allow for reaching a comfortable speed.

Secondly, we have investigated how pedestrians fill the available space. We considered a definition of density hinged on assigning to each pedestrian a personal space (circular, with radius  $R = 0.75$  m). We considered the total occupied area as the union of these personal spaces. We defined as density the ratio between the number of observed people and such area. Our choice of  $R$  yields a level-of-service for well separated pedestrians at the interface between level A (free-flow) and B (slightly restricted flow). This choice of  $R$  is however consistent with the sudden velocity reduction that we observe as a closest neighbour in front gets to a distance smaller than  $2R$ .

The total occupied area admits an upper bound defined by the (minimum between) the area of  $N$  disjoint personal areas (linear growth) and the total surface of the observed region. Notably pedestrians opt not to fill all the available space (differently, e.g., from a ideal gas) and even at relatively low density levels they occupy a smaller area than the concept of personal space would predict. It is interesting to notice that the occupied area immediately departs from a linear growth and approaches the total area of the facility only smoothly, as the number of pedestrians  $N$  grows. This is due to an interplay of different elements, including the presence of social groups (yielding people walking in proximity). We interpret this in terms of a compressibility factor,  $Z$ , of the crowd being smaller than 1 to represent attractive interactions (in analogy with similar effects in non-ideal gases). Most importantly we introduce a novel

parameter,  $p$ -value, that allows to quantitatively model the way pedestrians fill the available space. In the specific setting studied here we find that the area gets filled consistently with a value  $p = -2.5$ . This quantity expresses how smoothly the saturation capacity is reached (note that  $p = -\infty$  would yield an ideal gas-like behavior for which all the available space is used and pedestrians do not accept to compress until needed). In general we expect the  $p$ -value to correlate at least with cultural preferences, with the specific geometry, with the crowd composition and with the specific flow conditions. We believe that a deeper understanding of the  $p$ -value and its usage in crowd simulations will be key to reproduce realistic crowd dynamics scenarios and risk assessments.

Considering how the distance to the closest neighbors changes with density we observed that pedestrians strive to maintain a distance to their closest neighbor that is quasi elliptical in shape. We observed besides that the presence of pedestrians on closed proximity on the side would not influence the walking speed, that instead starts to diminish as the person in front gets closer than approximately  $2R$ . As a consequence, during our year-long measurement campaign we rarely observe configurations with density values larger than  $1.5 \text{ ped/m}^2$ , at variance with data from lab experiments and evacuation drills. We stress that the data collected during this period accurately reflects the typical traffic at a train station in the busiest railway network of Europe.

Finally, we have investigated the relationship between density and velocity under diverse flow conditions exploring complete probability distributions. We have shown that a key component for an accurate modeling of the probability, due to the presence of a significant tail at high velocity, is the consideration of a mixture of two Gaussian distributions. In both cases of ascending and descending pedestrians we have provided a linear parametrization of how the mean and the variance of these two components scale with density. We deem these parametrizations as key reference towards more accurate crowd simulation models and facility design.

Probabilities are vital in performance-based engineering, guiding the design of infrastructures to withstand potential extreme events. Our study facilitates the evaluation of staircase performance indicators, such as pedestrian flux, across a spectrum of probabilities. For instance, at probability 1%, 5%, and 10%, we expect flux reductions of 50%, 35%, and 30%, respectively. Capacity reductions of this kind can raise safety concerns with potential financial implications. This type of insights, attainable only through extensive real-life studies, underline the significance of high-statistics real-world measurements in engineering.

In future works, we plan to investigate the formation of queues at the top of escalators and staircase, which originate as people try to establish a comfort zone in order to safely descent in crowded configurations, and to establish stochastic quantitative models for the individual and ensemble dynamics.

## Acknowledgments

This work is supported by the HTSM research program “HTCrowd: a high-tech platform for human crowd flows monitoring, modeling and nudging” with project number 17962, financed by the Dutch Research Council (NWO). We acknowledge Gijs Mescher for his valuable contribution in the sensor calibration and fusion of depth images.

## Appendix

### A. YOLO for pedestrian localization on depth images

To the best of our knowledge, there are currently no publicly available datasets containing overhead pedestrian depth images suitable for our specific use case. Consequently, we constructed our own dataset to train the YOLO model. In this section we describe the process used to create and validate this dataset.

#### A.1. Dataset creation

We generate the dataset using an active learning cycle [Settles \(2009\)](#). Initially, we manually annotated approximately 100 pedestrians in 15 frames with low global densities. We crop the annotations at the edge of the bounding box and store these annotations as references. Subsequently, we insert a randomized quantity of these references into frames with existing annotations using a CutMix-like approach, allowing for a slight overlap (cf. [Yun, Han, Oh, Chun, Choe and Yoo \(2019\)](#)). By allowing this slight overlap, we aim to generate new and distinctive shapes that are similar to people being in proximity to each other, effectively augmenting our dataset. An example of this process can be seen in [Fig. 12](#). On this basis, we generate about 16000 images covering a range of density levels. These images serve as the training data set for the first training iteration of our YOLOv7 model.

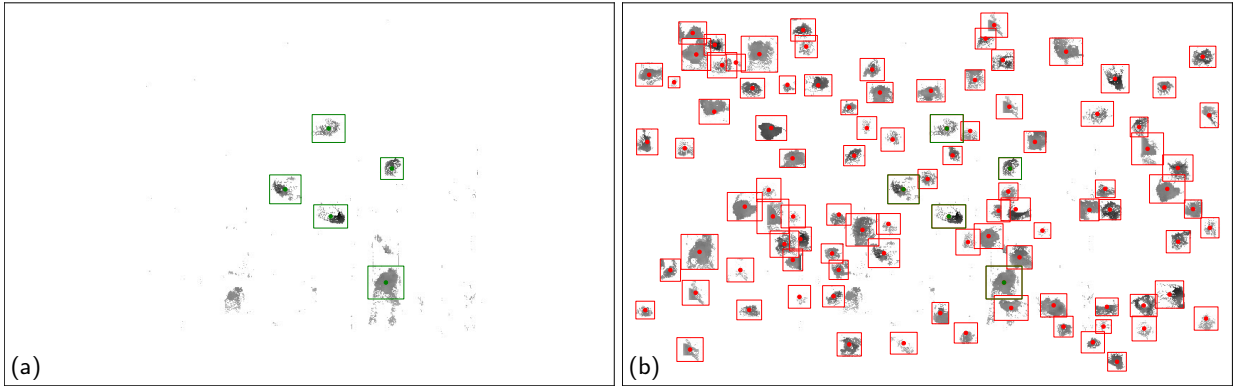


**Figure 12:** Example of an image in our CutMix-like approach to create an image for our training dataset. The green bounding boxes represent the original annotations, while the red bounding boxes represent the inserted reference annotations. (a) Original image with annotations. The non-annotated gray spots is noise that is present in the data. (b) Image with inserted reference annotations.

We utilize the resulting model to aid in the annotation of the next data set. The model generates initial annotations for new frames outside the existing dataset. We conduct a comprehensive review of these annotations, wherein we approve the correct annotations, add any missed annotations, and correct any erroneous annotations. The typical corrections that are made during the review process can be divided into three categories. The first category are straightforward false positives (Fig. 13a,d), in which the model incorrectly annotates a non-pedestrian as a pedestrian. The second category are straightforward false negatives (Fig. 13b,e), this involves instances where the model fails to detect pedestrians that are present in the frame. The final category represents a more intricate scenario where the model mistakenly identifies multiple pedestrians walking in proximity of each other as a single pedestrian (Fig. 13c,f), resulting in a false positive and multiple false negatives.

The iterative process of utilizing the previous model to assist in the creation of the next data set increases the efficiency at which we can create new annotations. We use the same CutMix-like approach to create the next dataset with the new annotations. A new model is trained on this dataset using transfer learning. We repeat this process until the model is sufficiently accurate. The final dataset consists of approximately 3700 annotations distributed across 819 images. Notably, this last dataset encompasses frames that capture a wider range of global density compared to the initial iteration of the data set.

## A.2. Pedestrian localization model validation

During the validations process, we quantify the accuracy of the model considering 500 frames outside the training dataset. To ensure a thorough evaluation, we select frames covering a diverse range of local densities. These frames are then divided into equally sized density bins, with each bin containing 100 images. We conduct a thorough review of the model-generated annotations, following the same correction process as during the dataset generation. In this validation, any erroneous annotations are considered false positives, while additional annotations are considered false negatives.

We assess the quality of the model by the precision ( $P_e$ ), recall ( $R_e$ ) and F1 score ( $F_1$ ) of the model using the reviewed frames, defined as follows:

$$P_e = \frac{T_P}{T_P + F_P}, \quad R_e = \frac{T_P}{T_P + F_N}, \quad F_1 = 2 \frac{P_e R_e}{P_e + R_e}, \quad (25)$$

where  $T_P$  is the number of true positives,  $F_P$  is the number of false positives and  $F_N$  is the number of false negatives. Precision indicates the fraction of correct detections with respect to the total number of detections, offering a measure of the quality of the detections. Recall denotes the fraction of correct detections with respect to the total number of expected detections, providing a measure of the quantity of relevant detections. The F1 score represents the harmonic mean of the precision and recall. In the ideal case of a perfect model all these parameters are equal to 1. We visualize the quality of the model through a precision-recall curve in Fig. 14. This curve, represented by ( $P_{[0.55-1.55]}$ ), illustrates the relationship between recall and precision for the evaluated local density domain, which ranges from 0.55 ped/m<sup>2</sup>

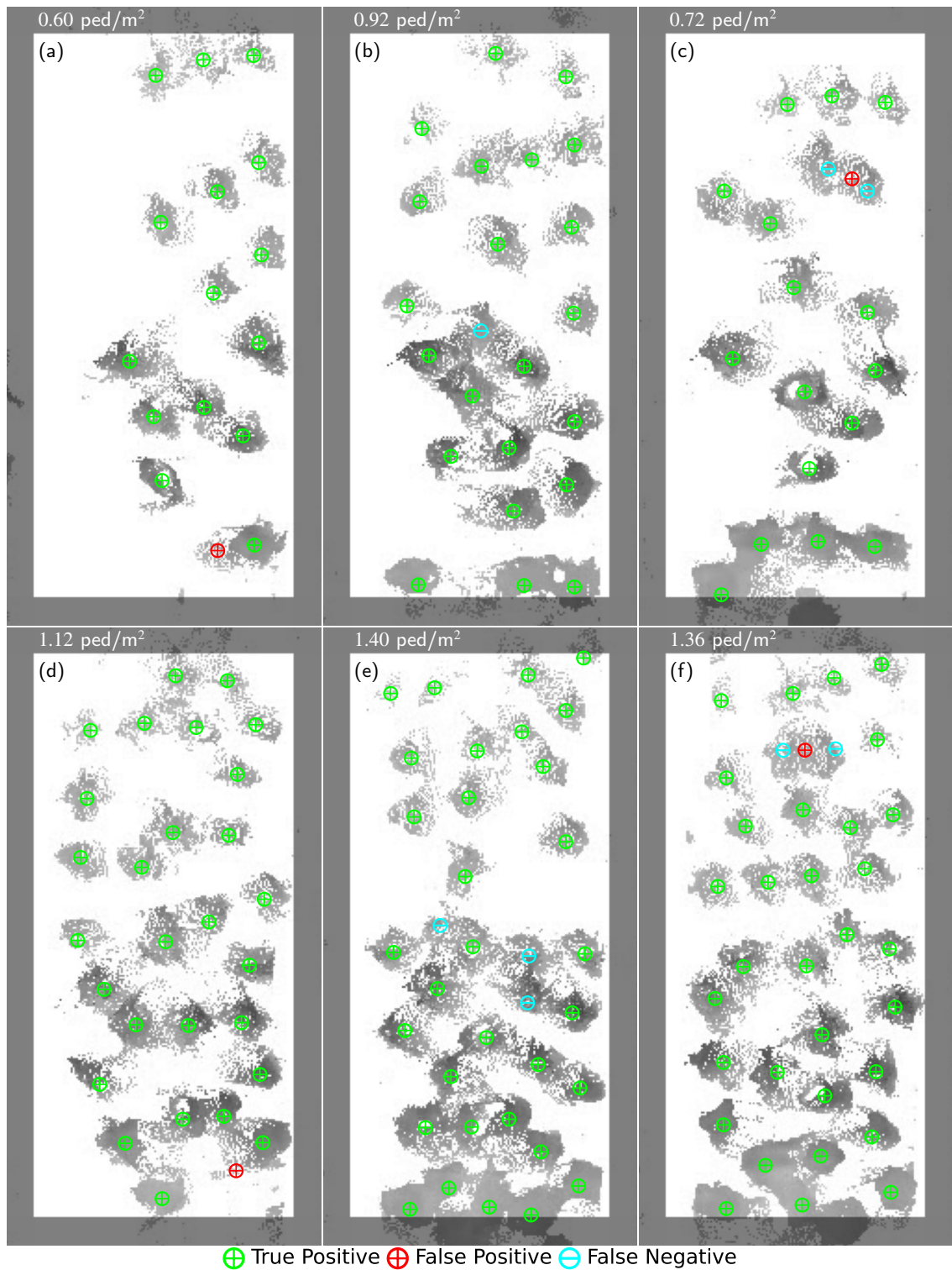


**Figure 13:** Typical corrections made during the model assisted annotations. Global density of the scenes are indicated at the top of each image. The bounding boxes are not displayed to improve readability. (a,d) Straightforward false positive. (b,e) Straightforward false negative. (c,f) Multiple pedestrians detected as a single pedestrian, resulting in a false positive and multiple false negatives.

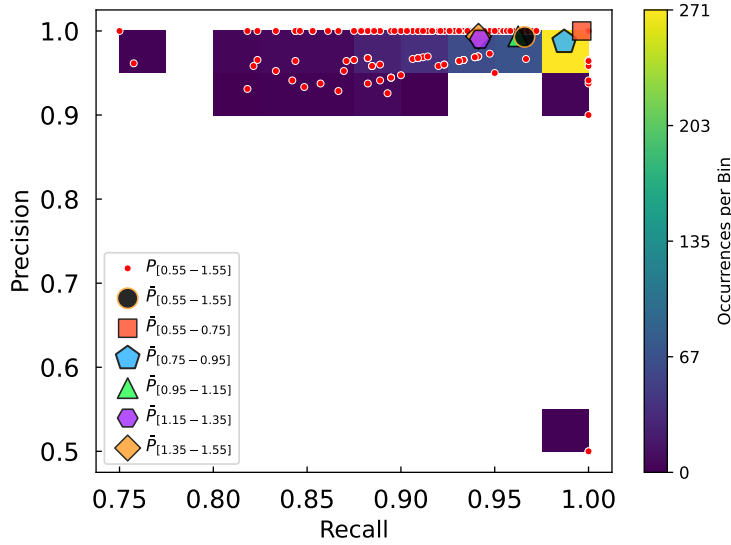


**Figure 14:** Precision-recall curve ( $P_{[0.55-1.55]}$ ) of our model, along with the mean precision-recall  $\bar{P}_{[0.55-1.55]}$ , and the number of occurrences per indicated precision-recall bin for the entire evaluated local density domain, ranging from 0.55 ped/m<sup>2</sup> to 1.55 ped/m<sup>2</sup> in 500 frames. The plot also includes the means ( $\bar{P}$ ) of the different evaluated density bins. Showcasing the exceptional accuracy of our model for densities below 0.95 ped/m<sup>2</sup>, while still performing commendably up to 1.55 ped/m<sup>2</sup>

to 1.55 ped/m<sup>2</sup>. Additionally, the mean precision-recall,  $\bar{P}_{[0.55-1.55]}$ , for this entire density domain is plotted, along with the means ( $\bar{P}$ ) of the different density bins. Finally, the number of occurrences per indicated precision-recall bin is displayed in the plot, showcasing the significant number of frames with both good precision and good recall.

Fig. 14 and Table 2 provide an overview of the performance of our model across various precision and recall levels. It demonstrates that our model exhibits exceptional accuracy for densities below 0.95 ped/m<sup>2</sup> and still performs extremely well for densities up to 1.55 ped/m<sup>2</sup>, which is close to the maximum local density recorded.

## B. Fundamental diagrams based on hydrodynamic density

Traditionally, the fundamental diagram is computed by employing the hydrodynamic definition from Eq. (7) to calculate the pedestrian density. In this work however, we estimate the pedestrian density as the ratio between the number of pedestrians and the union of all the personal spaces as defined in Eq. 9 for reasons elaborated in Sec. 2.3. This appendix provides a comparison between the classical method and the method employed in this work. In Fig. 15a we provide an example of a frame with  $N = 14$  pedestrians where the global area  $\bar{S} = 25$  m<sup>2</sup> is indicated by the orange colored domain. This example yields a hydrodynamic density  $\rho = 14/25 \approx 0.56$  ped/m<sup>2</sup>. In Fig. 15b we provide a comparison between the pedestrian density employed in this work  $N/\hat{S}_{stairs}$  and the classical density  $N/\bar{S}$  for increasing number of pedestrians  $N_{stairs}$ . We observe that our method has a lower bound determined by not intersecting personal spaces  $1/(\pi R^2) = 0.56$  m<sup>2</sup>. For increasing number of pedestrians we observe that our method converges to the classical approach. For comparison with the fundamental diagram from Fig. 10 we report the classical fundamental diagram in Fig. 15c,d.

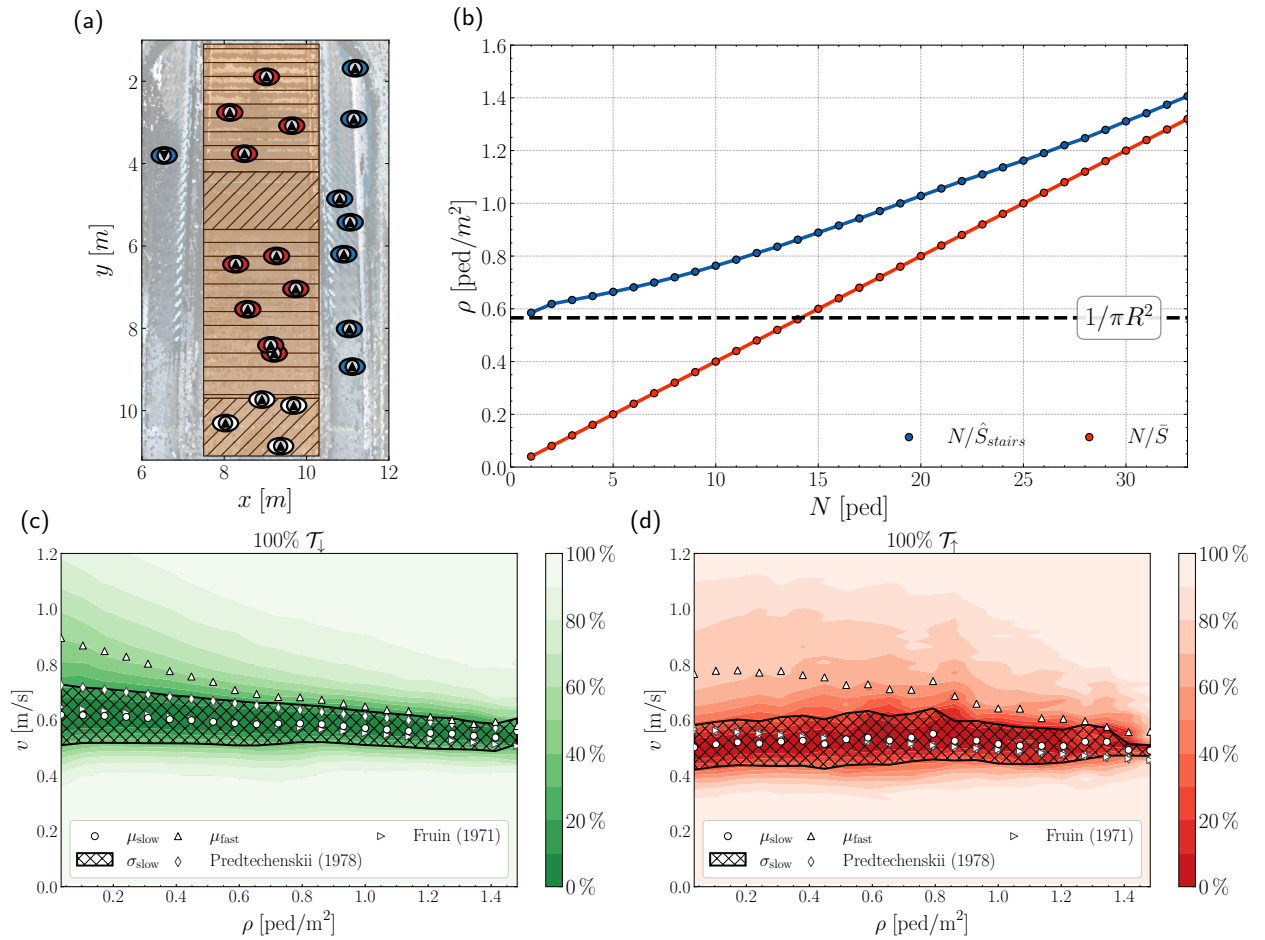


**Figure 15:** Fundamental diagram using the classical method to compute the crowd density. (a) Illustration of a frame with  $N = 14$  pedestrians. Global surface area used to calculate the density indicated with an orange color. (b) Comparison of the global density calculated using the classical method from Eq. (7) with  $A = 25 \text{ m}^2$ , and the local density calculation method from Eq. (9) (blue dots) (c) Classical fundamental diagram for unidirectional flow of descending pedestrians,  $100\% \mathcal{T}_{\downarrow}$ , and (d) for ascending pedestrians,  $100\% \mathcal{T}_{\uparrow}$ .

## References

- Allan, D.B., Caswell, T., Keim, N.C., van der Wel, C.M., Verweij, R.W., 2023. soft-matter/trackpy: v0.6.1. doi:10.5281/zenodo.7670439.
- Augusti, G., Ciampoli, M., 2008. Performance-based design in risk assessment and reduction. Probabilistic Engineering Mechanics 23, 496–508. URL: <https://www.sciencedirect.com/science/article/pii/S0266892008000313>, doi:<https://doi.org/10.1016/j.proengmech.2008.01.007>. dedicated to Professor Ove Ditlevsen.
- Bršćić, D., Zanlungo, F., Kanda, T., 2014. Density and velocity patterns during one year of pedestrian tracking. Transportation Research Procedia 2, 77–86. doi:10.1016/j.trpro.2014.09.011.
- Burghardt, S., Seyfried, A., Klingsch, W., 2013. Performance of stairs – fundamental diagram and topographical measurements. Transportation Research Part C: Emerging Technologies 37, 268–278. doi:10.1016/j.trc.2013.05.002.
- Cao, S., Lian, L., Chen, M., Yao, M., Song, W., Fang, Z., 2018. Investigation of difference of fundamental diagrams in pedestrian flow. Physica A: Statistical Mechanics and its Applications 506, 661–670. doi:10.1016/j.physa.2018.04.084.
- Cao, S., Sun, F., Chraïbi, M., Jiang, R., 2021. Spatial analysis for crowds in multi-directional flows based on large-scale experiments. Journal of Statistical Mechanics: Theory and Experiment 2021, 113407. URL: <https://dx.doi.org/10.1088/1742-5468/ac3660>, doi:10.1088/1742-5468/ac3660.
- Chen, J., Hao, Y., Wang, J., Wang, P., Liu, X., Lin, P., 2018. An experimental study of ascent and descent movement of people on long stair with high occupying density. Fire technology 54, 1683–1704. doi:10.1007/s10694-018-0759-2.
- Chen, J., Lo, S.M., Ma, J., 2017. Pedestrian ascent and descent fundamental diagram on stairway. Journal of Statistical Mechanics: Theory and Experiment 2017, 083403. doi:10.1088/1742-5468/aa79ad.
- Corbetta, A., Bruno, L., Muntean, A., Toschi, F., 2014. High statistics measurements of pedestrian dynamics. Transportation Research Procedia 2, 96–104. doi:10.1016/j.trpro.2014.09.013.

- Corbetta, A., Lee, C.m., Benzi, R., Muntean, A., Toschi, F., 2017. Fluctuations around mean walking behaviors in diluted pedestrian flows. *Phys. Rev. E* 95, 032316. doi:10.1103/PhysRevE.95.032316.
- Corbetta, A., Meeseusen, J.A., Lee, C.m., Benzi, R., Toschi, F., 2018. Physics-based modeling and data representation of pairwise interactions among pedestrians. *Phys. Rev. E* 98, 062310. doi:10.1103/PhysRevE.98.062310.
- Corbetta, A., Toschi, F., 2023. Physics of human crowds. *Annual Review of Condensed Matter Physics* 14, 311–333. doi:10.1146/annurev-conmatphys-031620-100450.
- Cristiani, E., Piccoli, B., Tosin, A., 2014. *Multiscale modeling of pedestrian dynamics*. volume 12. Springer.
- Drury, J., 2020. Recent developments in the psychology of crowds and collective behaviour. *Current Opinion in Psychology* 35, 12–16. doi:10.1016/j.copsyc.2020.02.005. social Change (Rallies, Riots and Revolutions).
- Duives, D.C., Daamen, W., Hoogendoorn, S.P., 2015. Quantification of the level of crowdedness for pedestrian movements. *Physica A: Statistical Mechanics and its Applications* 427, 162–180. doi:10.1016/j.physa.2014.11.054.
- European Committee for Standardization, 2002. NEN EN1990:2002 Eurocode — Basis of structural design. Standard. European Committee for Standardization.
- Feliciani, C., Corbetta, A., Haghani, M., Nishinari, K., 2023. Trends in crowd accidents based on an analysis of press reports. *Safety Science* 164, 106174. doi:10.1016/j.ssci.2023.106174.
- Frantzich, H., 1996. Study of movement on stairs during evacuation using video analysing techniques. Lund University, Institute of Technology, Department of Fire Safety Engineering.
- Fruin, J.J., 1971. *Pedestrian planning and design*. Elevator World, New York.
- Fujiyama, T., Tyler, N., 2004. An explicit study on walking speeds of pedestrians on stairs, in: in *Proc. 10th International Conference on Mobility and Transport for Elderly and Disabled People (TRANSED 2004)*, pp. 643–652. Free-flow, normal and fast walking speed.
- Gabbana, A., Toschi, F., Ross, P., Haans, A., Corbetta, A., 2022. Fluctuations in pedestrian dynamics routing choices. *PNAS Nexus* 1. doi:10.1093/pnasnexus/pgac169.
- Gérin-Lajoie, M., Richards, C.L., Fung, J., McFadyen, B.J., 2008. Characteristics of personal space during obstacle circumvention in physical and virtual environments. *Gait & Posture* 27, 239–247. doi:10.1016/j.gaitpost.2007.03.015.
- Haghani, M., 2021. The knowledge domain of crowd dynamics: Anatomy of the field, pioneering studies, temporal trends, influential entities and outside-domain impact. *Physica A: Statistical Mechanics and its Applications* 580, 126145. doi:10.1016/j.physa.2021.126145.
- Hall, E.T., 1966. *The Hidden Dimension*. Anchor Books NY.
- Hankin, B., Wright, R.A., 1958. Passenger flow in subways. *Journal of the Operational Research Society* 9, 81–88. doi:10.1057/jors.1958.9.
- Hoogendoorn, S., Daamen, W., Knoop, V., Steenbakkens, J., Sarvi, M., 2018. Macroscopic fundamental diagram for pedestrian networks: Theory and applications. *Transportation Research Part C: Emerging Technologies* 94, 172–184. doi:10.1016/j.trc.2017.09.003. iSTTT22.
- Hughes, R.L., 2003. The flow of human crowds. *Annual review of fluid mechanics* 35, 169–182.
- Jackson, P.L., Cohen, H., 1995. An in-depth investigation of 40 stairway accidents and the stair safety literature. *Journal of Safety Research* 26, 151–159. doi:10.1016/0022-4375(95)00014-H.
- Köster, G., Lehmborg, D., Kneidl, A., 2019. Walking on stairs: Experiment and model. *Phys. Rev. E* 100, 022310. doi:10.1103/PhysRevE.100.022310.
- Kretz, T., Grünebohm, A., Kessel, A., Klüpfel, H., Meyer-König, T., Schreckenberg, M., 2008. Upstairs walking speed distributions on a long stairway. *Safety Science* 46, 72–78. doi:10.1016/j.ssci.2006.10.001.
- Lam, W.H.K., Cheung, C.Y., 2000. Pedestrian speed/flow relationships for walking facilities in hong kong. *Journal of Transportation Engineering* 126, 343–349. doi:10.1061/(ASCE)0733-947X(2000)126:4(343).
- Ma, J., Song, W., Tian, W., Lo, S., Liao, G., 2012. Experimental study on an ultra high-rise building evacuation in china. *Safety Science* 50, 1665–1674. doi:10.1016/j.ssci.2011.12.018. evacuation and Pedestrian Dynamics.
- Moussaïd, M., Guillot, E.G., Moreau, M., Fehrenbach, J., Chabiron, O., Lemerrier, S., Petré, J., Appert-Rolland, C., Degond, P., Theraulaz, G., 2012. Traffic instabilities in self-organized pedestrian crowds. *PLOS Computational Biology* 8, 1–10. doi:10.1371/journal.pcbi.1002442.
- NVIDIA, 2021. *Nvidia jetson tx2 nx system-on-module*. URL: <https://developer.nvidia.com/embedded/jetson-tx2>.
- Peacock, R., Hoskins, B., Kuligowski, E., 2012. Overall and local movement speeds during fire drill evacuations in buildings up to 31 stories. *Safety Science* 50, 1655–1664. doi:10.1016/j.ssci.2012.01.003. evacuation and Pedestrian Dynamics.
- Pouw, C.A.S., Toschi, F., van Schadewijk, F., Corbetta, A., 2020. Monitoring physical distancing for crowd management: Real-time trajectory and group analysis. *PLoS ONE* 15, 1–18. doi:10.1371/journal.pone.0240963.
- Pouw, C.A.S., Willems, J., van Schadewijk, F., Thureau, J., Toschi, F., Corbetta, A., 2022. Benchmarking high-fidelity pedestrian tracking systems for research, real-time monitoring and crowd control. *Collective Dynamics* 6, 1–22. doi:10.17815/CD.2021.134.
- Predtecheskii, V.M., Milinskii, A.I., 1978. Planning for foot traffic flow in buildings. Amerind.
- ProRail, 2021. *Transferongevallen - jaarverslag 2021*. Technical Report. ProRail. URL: <https://www.jaarverslagprorail.nl/jaarverslag-2021/spoorprestaties/veiligheid/veilig-reizen>.
- Qu, Y., Gao, Z., Xiao, Y., Li, X., 2014. Modeling the pedestrian's movement and simulating evacuation dynamics on stairs. *Safety Science* 70, 189–201. doi:10.1016/j.ssci.2014.05.016.
- Ren, X., Zhang, J., Song, W., 2019. Contrastive study on the single-file pedestrian movement of the elderly and other age groups. *Journal of Statistical Mechanics: Theory and Experiment* 2019, 093402. doi:10.1088/1742-5468/ab39da.
- Ronchi, E., Norén, J., Delin, M., Kuklane, K., Halder, A., Arias, S., Fridolf, K., 2016. Ascending evacuation in long stairways: Physical exertion, walking speed and behaviour. Department of Fire Safety Engineering and Systems Safety, Lund University.
- Saberi, M., Aghabayk, K., Sobhani, A., 2015. Spatial fluctuations of pedestrian velocities in bidirectional streams: Exploring the effects of self-organization. *Physica A: Statistical Mechanics and its Applications* 434, 120–128. doi:https://doi.org/10.1016/j.physa.2015.04.008.
- Saberi, M., Mahmassani, H.S., 2014. Exploring areawide dynamics of pedestrian crowds: Three-dimensional approach. *Transportation Research Record* 2421, 31–40. doi:10.3141/2421-04.

- Savitzky, A., Golay, M.J., 1964. Smoothing and differentiation of data by simplified least squares procedures. *Analytical chemistry* 36, 1627–1639. doi:10.1098/rsif.2022.0061.
- Seer, S., Brändle, N., Ratti, C., 2014. Kinects and human kinetics: A new approach for studying pedestrian behavior. *Transport. Res. C-Emer.* 48, 212–228. doi:10.1016/j.trc.2014.08.012.
- Settles, B., 2009. Active learning literature survey.
- Shi, D., Ma, J., Luo, Q., Li, X., Chen, J., Lin, P., 2021. Fundamental diagrams of luggage-laden pedestrians ascending and descending stairs. *Physica A: Statistical Mechanics and its Applications* 572, 125880. doi:10.1016/j.physa.2021.125880.
- Spoorwegen, N., 2023. Eindhoven Centraal - Jaarverslag 2019-2022. Technical Report. NS Groep. URL: <https://dashboards.nsjaarverslag.nl/reizigersgedrag/eindhoven-centraal>.
- Steffen, B., Seyfried, A., 2010. Methods for measuring pedestrian density, flow, speed and direction with minimal scatter. *Physica A: Statistical Mechanics and its Applications* 389, 1902–1910. doi:10.1016/j.physa.2009.12.015.
- Stereolabs, 2021. Zed 2 camera and sdk overview. URL: <https://www.stereolabs.com/assets/datasheets/zed2-camera-datasheet.pdf>.
- Subaih, R., Maree, M., Chraïbi, M., Awad, S., Zanoon, T., 2019. Gender-based insights into the fundamental diagram of pedestrian dynamics, in: Nguyen, N.T., Chbeir, R., Exposito, E., Anioté, P., Trawiński, B. (Eds.), *Computational Collective Intelligence*, Springer International Publishing, Cham. pp. 613–624.
- Subaih, R., Maree, M., Tordeux, A., Chraïbi, M., 2022. Questioning the anisotropy of pedestrian dynamics: An empirical analysis with artificial neural networks. *Applied Sciences* 12. doi:10.3390/app12157563.
- Templer, J., 1995. *The staircase: studies of hazards, falls, and safer design*. volume 2. MIT press.
- Van Toll, W., Triesscheijn, R., Kallmann, M., Oliva, R., Pelechano, N., Pettré, J., Geraerts, R., 2016. A comparative study of navigation meshes, in: *Proceedings of the 9th International Conference on Motion in Games*, pp. 91–100.
- Vanumu, L.D., Tiwari, K.R.R.G., 2017. Fundamental diagrams of pedestrian flow characteristics: A review. *European Transport Research Review* 9. doi:10.1007/s12544-017-0264-6.
- Wang, C.Y., Bochkovskiy, A., Liao, H.Y.M., 2022. YOLOv7: Trainable bag-of-freebies sets new state-of-the-art for real-time object detectors. arXiv preprint arXiv:2207.02696.
- Wang, J., Ma, J., Lin, P., Sarvi, M., Li, R., 2021. Pedestrian single file movement on stairway: Investigating the impact of stair configuration on pedestrian ascent and descent fundamental diagram. *Safety Science* 143, 105409. doi:10.1016/j.ssci.2021.105409.
- Willems, J., Corbetta, A., Menkovski, V., Toschi, F., 2020. Pedestrian orientation dynamics from high-fidelity measurements. *Scientific reports* 10, 1–10. doi:10.1038/s41598-020-68287-6.
- Xie, C.Z., Tang, T.Q., Zhang, B.T., Nicolas, A., 2023. Adult–child pairs walking down stairs: empirical analysis and optimal-step-based modeling of a complex pedestrian flow, with an exploration of flow-improvement strategies. *Journal of Statistical Mechanics: Theory and Experiment* 2023, 013404. URL: <https://dx.doi.org/10.1088/1742-5468/acb25f>, doi:10.1088/1742-5468/acb25f.
- Ye, J., Chen, X., Yang, C., Wu, J., 2008. Walking behavior and pedestrian flow characteristics for different types of walking facilities. *Transportation Research Record* 2048, 43–51. doi:10.3141/2048-06.
- Ye, R., Fang, Z., Zeng, G., Wang, Q., Lian, L., Cao, S., 2023. Characteristics of pedestrians descending on a stairway: A trajectory-based empirical analysis. *Safety Science* 160, 106068. doi:10.1016/j.ssci.2023.106068.
- Ye, R., Zeng, Y., Zeng, G., Huang, Z., Li, X., Fang, Z., Song, W., 2021. Pedestrian single-file movement on stairs under different motivations. *Physica A: Statistical Mechanics and its Applications* 571, 125849. doi:10.1016/j.physa.2021.125849.
- Yun, S., Han, D., Oh, S.J., Chun, S., Choe, J., Yoo, Y., 2019. Cutmix: Regularization strategy to train strong classifiers with localizable features. arXiv preprint arXiv:1905.04899 doi:10.48550/ARXIV.1905.04899.
- Zanlungo, F., Ikeda, T., Kanda, T., 2014. Potential for the dynamics of pedestrians in a socially interacting group. *Phys. Rev. E* 89, 012811. doi:10.1103/PhysRevE.89.012811.
- Zhang, J., Klingsch, W., Schadschneider, A., Seyfried, A., 2011. Transitions in pedestrian fundamental diagrams of straight corridors and t-junctions. *Journal of Statistical Mechanics: Theory and Experiment* 2011, P06004. doi:10.1088/1742-5468/2011/06/P06004.
- Zucker, R., Bilblarz, O., 2019. *Fundamentals of Gas Dynamics*. Wiley.